AFGL-TR- 88-0030
INSTRUMENTATION PAPERS, NO. 335

Precipitating Ion and Electron Detectors (SSJ/4) for the Block 5D/Flight 8 DMSP Satellite

T.L. SCHUMAKER
D.A. HARDY
S. MORAN
A. HUBER
J. McGARITY
J. PANTAZIS

4 February 1988

SPACE PHYSICS DIVISION PROJECT 7601

AIR FORCE GEOPHYSICS LABORATORY

HANSCOM AFB, MA 01731

Unclassified

SECURITY CLASSIFICATION OF THIS PAGE

REPORT DOCUMENTATION PAGE

Form Approved OMB No. 0704-0188

1a. REPORT SECURITY CLASSIFICATION Unclassified	1b. RESTRICTIVE MARKINGS
2a. SECURITY CLASSIFICATION AUTHORITY	3. DISTRIBUTION/AVAILABILITY OF REPORT Approved for public release; distribution unlimited.
2b. DECLASSIFICATION/DOWNGRADING SCHEDULE	
4. PERFORMING ORGANIZATION REPORT NUMBER(S) AFGL-TR-88-0030 IP, No. 335	5. MONITORING ORGANIZATION REPORT NUMBER(S)
6a. NAME OF PERFORMING ORGANIZATION Air Force Geophysics Laboratory 6b. OFFICE SYMBOL (*If applicable*) PHP	7a. NAME OF MONITORING ORGANIZATION
6c. ADDRESS (*City, State, and ZIP Code*) Hanscom AFB Massachusetts 01731-5000	7b. ADDRESS (*City, State, and ZIP Code*)
8a. NAME OF FUNDING/SPONSORING ORGANIZATION 8b. OFFICE SYMBOL (*If applicable*)	9. PROCUREMENT INSTRUMENT IDENTIFICATION NUMBER
8c. ADDRESS (*City, State, and ZIP Code*)	10. SOURCE OF FUNDING NUMBERS

PROGRAM ELEMENT NO.	PROJECT NO.	TASK NO.	WORK UNIT ACCESSION NO.
62101F	7601	760122	75012201

11. TITLE (*Include Security Classification*)
Precipitating Ion and Electron Detectors (SSJ/4) for the Block 5D/Flight 8 DMSP Satellite

12. PERSONAL AUTHOR(S)
T. L. Schumaker*, D.A. Hardy, S. Moran**, A. Huber**, J. McGarity**, & J. Pantazis**

13a. TYPE OF REPORT	13b. TIME COVERED	14. DATE OF REPORT (*Year, Month, Day*)	15. PAGE COUNT
Scientific. Interim.	FROM _____ TO _____	1988 February 4	60

16. SUPPLEMENTARY NOTATION
*AFGL-SCEEE Geophysics Scholar Program, AFGL/PHP, Hanscom AFB, MA 01731
**Amptek, Inc., Bedford, MA 01730

17. COSATI CODES			18. SUBJECT TERMS (*Continue on reverse if necessary and identify by block number*)
FIELD	GROUP	SUB-GROUP	Defense meteorological satellite program (DMSP) Aurora Precipitating ions and electrons

19. ABSTRACT (*Continue on reverse if necessary and identify by block number*)

The satellites of the Defense Meteorological Satellite Program (DMSP) are flown operationally to provide data for the specification of terrestrial weather and near-Earth space environment. In support of space environment specifications, the satellites, starting with Flight 6 (F6), carry an improved set of electrostatic analyzers (SSJ/4). These instruments are designed to measure the flux of precipitating electrons and ions with energies between 30 eV and 30 keV. The data from these analyzers are routinely processed at the Air Force Geophysics Laboratory (AFGL) and are available to the scientific community. A description of the SSJ/4 electrostatic analyzers for the DMSP satellite, results of the extensive calibration of the instruments, and examples of data use are given in this report. The report was prepared to facilitate the widespread use of the SSJ/4 data. Both by itself, and in combination with other sensors on the satellite, the SSJ/4 detectors provide important data for the study of auroral processes.

20. DISTRIBUTION/AVAILABILITY OF ABSTRACT	21. ABSTRACT SECURITY CLASSIFICATION
☐ UNCLASSIFIED/UNLIMITED ☒ SAME AS RPT. ☐ DTIC USERS	Unclassified

22a. NAME OF RESPONSIBLE INDIVIDUAL	22b. TELEPHONE (*Include Area Code*)	22c. OFFICE SYMBOL
D.A. Hardy	(617) 377-3211	PHP

DD Form 1473, JUN 86 *Previous editions are obsolete.* SECURITY CLASSIFICATION OF THIS PAGE

Unclassified

Contents

Illustrations

Tables

Tables

Precipitating Ion and Electron Detectors (SSJ/4) for the Block 5D/Flight 8 DMSP Satellite

1. INTRODUCTION

The Defense Meteorological Satellite Program (DMSP) of the U.S. Air Force is principally devoted to providing data for the specification of terrestrial weather and the near-earth space environment. The program calls for two satellites to be in polar orbit at all times: one in the dawn-dusk meridian and one in the 1030 to 2230 meridian. Depending on launch dates and system lifetimes, there can be as many as three or as few as one satellite in operation at a given time.

Since 1974, sensors to measure precipitating auroral particles have been placed on the satellites in the DMSP program. The satellites are three axis stabilized and the sensors are oriented on the satellite with their look direction toward the local zenith, so that at auroral and polar cap latitudes they detect precipitating rather than backscattered and/or trapped particles. The original electrostatic analyzers measured electrons in six channels from 0.2 to 20 keV. With the launch of DMSP-F2 in June 1977, these were replaced by the SSJ/3 detectors, a set of two electrostatic analyzers covering the range 50 eV to 20 keV

(Received for publication 3 February 1988)

in 16 energy channels. The SSJ/3 detectors were also flown on the F3 through F5 satellites (Hardy et al[1]). Starting with the DMSP F6 and F7 flights (launched in December 1982 and November 1983, respectively), additional electrostatic analyzers were added to measure the flux of precipitating ions. Furthermore, for these new SSJ/4 detectors the energy range was extended to 30 eV on the low end and to 30 keV on the high end, and the number of channels was increased to 20. Such SSJ/4 detectors are planned for the F9 through F15 DMSP satellites.

The DMSP satellites are launched into a circular polar orbit with an altitude of 830 to 840 km and a period of approximately 101 minutes. The orbits have an inclination of 98.3° and are sun-synchronous in the dawn-dusk (F6 and F8) or 1030 to 2230 MLT (F7) meridians.

Because of the enormous volume and consistently high quality of the precipitating ion and electron measurements on the DMSP satellites, these data were used in several large statistical studies to specify average global auroral properties. Global maps of particle precipitation were determined as functions of magnetic local time, corrected geomagnetic latitude, and Kp magnetic index (Hardy et al[2,3]). Not only are these useful for verification of large-scale simulations of magnetospheric dynamics, but they also provide important information on ionospheric-magnetospheric coupling. The global maps were used as input codes that specify both height-integrated and height-varying Hall and Pederson conductivities as functions of time, season, and magnetic activity. Both the global maps of the precipitation pattern and conductivities were fit to simple functional forms, and were incorporated into operational software for the Air Force Global Weather Control.

---

1. Hardy, D.A., Gussenhoven, M.S., and Huber, A. (1979) The Precipitating Electron Detectors (SSJ/3) for the Block 5D/Flights 2 - 5 DMSP Satellites: Calibration and Data Reduction, AFGL-TR-79-0210, ADA 083136, Air Force Geophysics Laboratory, Hanscom AFB, MA.
2. Hardy, D.A., Gussenhoven, M.S., and Holeman, E. (1985) A statistical model of auroral electron precipitation, J. Geophys. Res., 90:4229.
3. Hardy, D.A., Gussenhoven, M.S., and Brautigam, D. (1988) A statistical model of auroral ion precipitation, to be published in J. Geophys. Res.

The variation of the equatorward electron and ion boundary of the diffuse aurora was found to be so regular with existing magnetic activity indices (Gussenhoven et al;[4,5,6] Hardy et al[7]) that by accounting for the auroral oval offset in local time, the boundary can be used, in turn, to specify auroral activity. An algorithm to automatically select the equatorward boundary from the DMSP electron data (Hardy and MacKean;[8] Gussenhoven et al[9]) is now used by Global Weather Central of the U.S. Air Force to produce a real time measure of auroral activity.

The DMSP data were also used to determine the statistical morphology of electron precipitation within the polar cusp, the polar cleft, and polar cap (Gussenhoven et al;[10,11] Hardy;[12] Hardy et al;[13] Riehl and Hardy[14]); to initially identify

---

4. Gussenhoven, M.S., Hardy, D.A., and Burke, W.J. (1981) DMSP/F2 electron observations of equatorward auroral boundaries and their relationship to magnetospheric electric fields, J. Geophys. Res., 86:768.
5. Gussenhoven, M.S., Hardy, D.A., and Heinemann, N. (1983) Systematics of the equatorward diffuse auroral boundary, J. Geophys. Res., 88:5692.
6. Gussenhoven, M.S., Hardy, D.A., and Heinemann, N. (1987) The equatorward boundary of auroral ion precipitation, J. Geophys. Res., 92:8273.
7. Hardy, D.A., Burke, W.J., Gussenhoven, M.S., Heinemann, N., and Holeman, E. (1981) DMSP/F2 electron observations of equatorward auroral boundaries and their relationship to the solar wind velocity and the north-south component of the interplanetary magnetic field, J. Geophys. Res., 86:9961.
8. Hardy, D.A., and MacKean, R. (1980) An Algorithm for Determining the Boundary of Auroral Precipitation Using Data from the SSJ/3 Sensor, AFGL-TR-80-0028, ADA 084482, Air Force Geophysics Laboratory, Hanscom AFB, MA.
9. Gussenhoven, M.S., Hardy, D.A., Heinemann, N., and Holeman, E. (1982) 1978 Diffuse Auroral Boundaries and a Derived Auroral Boundary Index, AFGL-TR-82-0398, ADA 130175, Air Force Geophysics Laboratory, Hanscom AFB, MA.
10. Gussenhoven, M.S., Hardy, D.A., Heinemann, N., and Burkhardt, R. (1984) Morphology of the polar rain, J. Geophys. Res., 89:9785.
11. Gussenhoven, M.S., Hardy, D.A., and Carovillano, R.L. (1985a) Average electron precipitation in the polar cusps, cleft, and cap in The Polar Cusp, (J.A. Holtet and A. Egeland, Eds.), D. Reidel Pub. Co., Holland, p. 85.
12. Hardy, D.A. (1984) Intense fluxes of low-energy electrons at geomagnetic latitudes above 85°, J. Geophys. Res., 89:3883.
13. Hardy, D.A., Gussenhoven, M.S., Riehl, K., Burkhardt, R., Heinemann, N., and Schumaker, T.L. (1986) The characteristics of polar cap precipitation and their dependence on the interplanetary magnetic field and the solar wind, in Solar Wind-Magnetospheric Coupling, (Y. Kamide and J.A. Slavin, Eds.), Terra Sci. Pub. Co., Tokyo, p. 575.
14. Riehl, K.B., and Hardy, D.A. (1986) Average characteristics of the polar rain and their relationship to the solar wind and interplanetary magnetic field, J. Geophys. Res., 91:1557.

ion signatures in polar crossings of the DMSP F6 and F7 satellites during periods of polar rain precipitation (Schumaker et al;[15] Hardy et al[13]); and to identify the charging events on the DMSP satellites (Gussenhoven et al;[16] Yeh and Gussenhoven[17]).

The calibration values of the SSJ/4 electron detectors for the DMSP F6, F7, F8, and F10 flights and the ion detectors for the F6 and F7 flights were reported by Hardy et al.[18] The Air Weather Service decided to launch the originally designated F9 satellites as F8. Since the SSJ/4 detector on the F9 satellite had been at the satellite contractor for more than 18 months, the detector was returned to AFGL for replacement of the channel electron multipliers (CEMs) prior to launch. The refurbished F9 detector was launched on the DMSP F8 satellite on 19 June 1987, and in the remainder of this report, will be referred to as the F8 detector.

Because of the unavailability of an ion beam source, the ion detectors were not directly calibrated. Instead, a combination of electron calibration results and in-flight data are used to assign ion geometric factors. Details of the derivation of ion detector calibration values are presented in Section 4.

2. DESCRIPTION OF THE SSJ/4 F8 DETECTOR

The SSJ/4 detector flown on the F8 satellite measures the precipitating flux of electrons and ions incident to the spacecraft in 20 channels logarithmically spaced in energy from 30 eV to 30 keV. This is accomplished using a set of four cylindrical curved plate electrostatic analyzers arranged in two pairs. In each pair, one analyzer uses cylindrical plates with a radius of curvature of 127°, and the other with a radius of curvature of 60°. A photograph of one pair of analyzers is shown in Figure 1. The voltage on the two sets of curved plates are sequenced through ten levels in tandem (from high voltage to low) such that for the 127° (60°) analyzers particles are sampled in energy channels from 1 keV to 30 eV (30 keV to 1 keV).

---

15. Schumaker, T.L., Gussenhoven, M.S., and Hardy, D.A. (1984) Ion signatures in the polar rain, EOS Trans. Am. Geophys. Union, 65:1065.

16. Gussenhoven, M.S., Hardy, D.A., Rich, F., Burke, W.J., and Yeh, H.-C. (1985b) High-level spacecraft charging in the low-altitude polar auroral environment, J. Geophys. Res., 90:11,009.

17. Yeh, H.-C., and Gussenhoven, M.S. (1987) The statistical electron environment for DMSP charging, J. Geophys. Res., 92:7705.

18. Hardy, D.A., Schmitt, L.K., Gussenhoven, M.S., Marshall, F.J., Yeh, Y.-C., Schumaker, T.L., Huber, A., and Pantazis, J. (1984) Precipitating Electron and Ion Detectors (SSJ/4) for the Block 5D/Flights 6 - 10 DMSP Satellites: Calibration and Data Presentation, AFGL-TR-84-0317, ADA 157080, Air Force Geophysics Laboratory, Hanscom AFB, MA.

The detector dwells for a period of 98 msec in each energy channel with a 2-msec period between steps to stabilize the voltage. The two analyzers are stepped together so that a complete 20-point ion and electron spectrum is returned once per second. Details of the configuration of the apertures and curved plates of an SSJ/4 analyzer are shown in Figure 2.

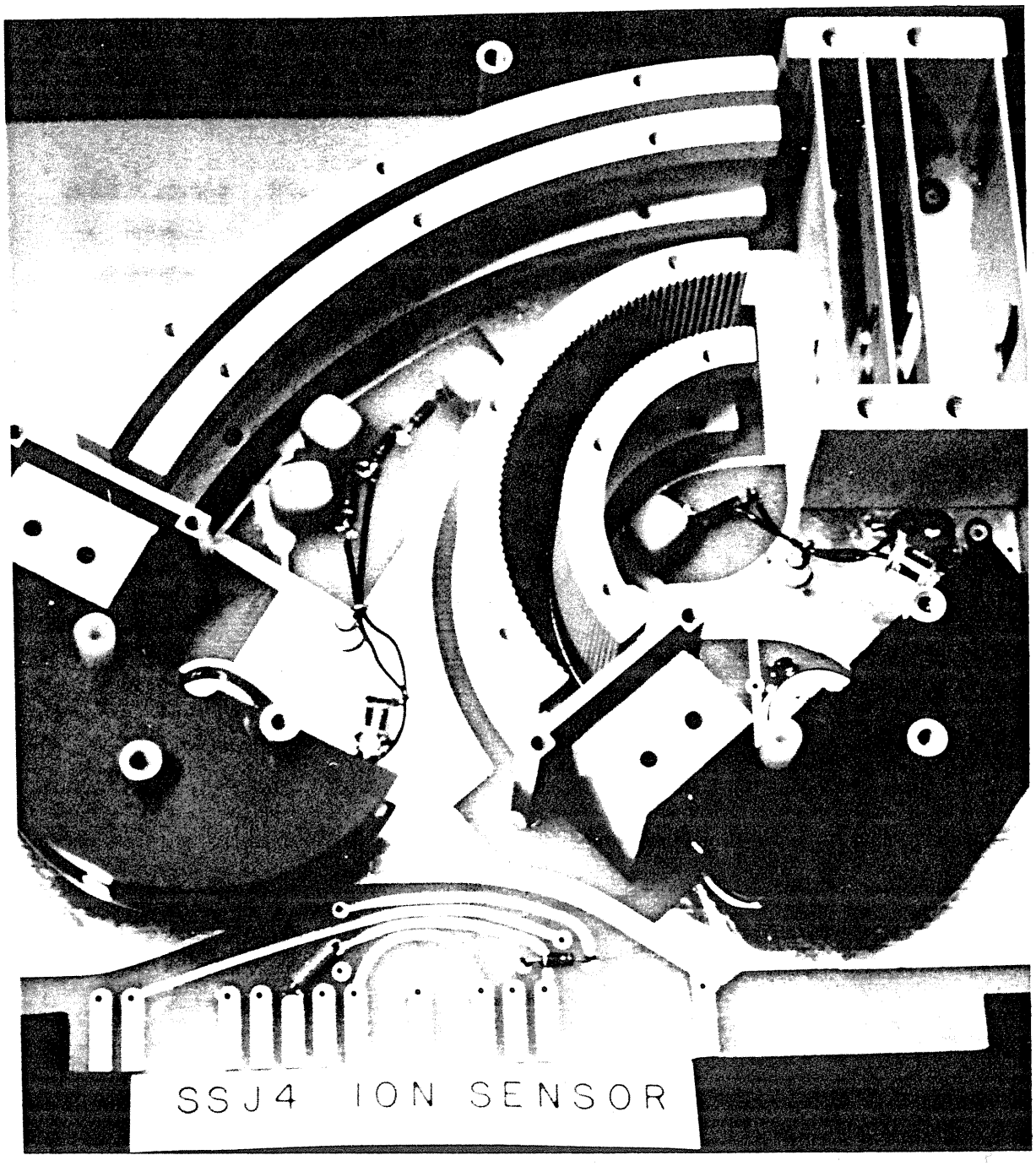

Figure 1. Photograph of Two Sensor Heads of the SSJ/4 Electrostatic Analyzer

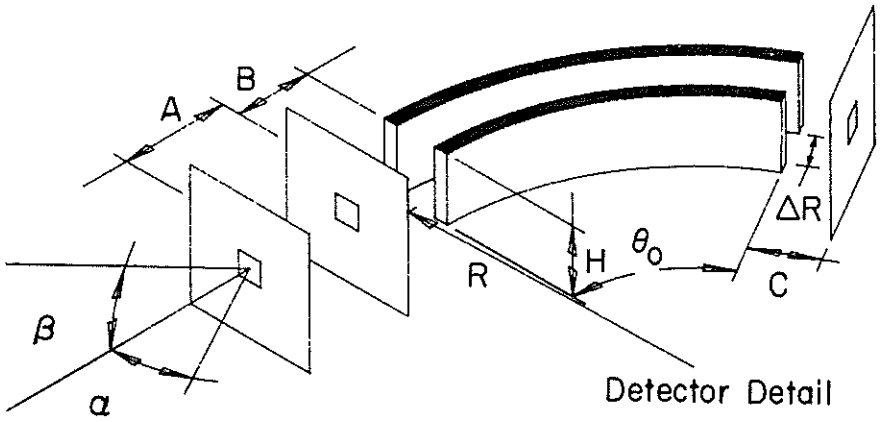

NOTE: Three apertures identical

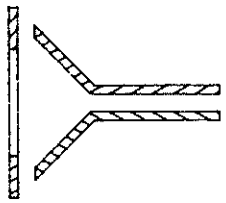

	High Energy ESA	Low Energy ESA
A – Telescope Length	1.15 cm	1.88 cm
B – Telescope to ESA	0.36	1.75
C – ESA to Exit Ap.	0.25	0.75
H – Plate Height	2.85	2.85
ΔR – Plate Separation	0.25	0.75
R – Mean Plate Radius	10.01	3.00
θ_0 – Plate Arc	60°	127°
Aperture Width	0.20	0.20 (Electron) 0.51 (Ion)
Aperture Height	1.80	0.60 (Electron) 1.59 (Ion)
Detectors, Cone Dia.	1.09	0.38 (Electron) 1.09 (Ion)

Figure 2. Details of the Configuration of the Aperture and Curved Plates of an SSJ/4 Electrostatic Analyzer

Both electron and ion detectors employ post-acceleration (100 V for electrons; 1 kV for ions) to insure unit CEM efficiency at low energies. The analyzers for ions and electrons are identical except that the polarity of the voltage on the plates are opposite and the low energy ion apertures are larger than the low energy electron apertures. The total SSJ/4 sensor package weighs 5 lbs and consumes 0.25 W of power.

In order to provide greater consistency in the SSJ/4 measurements, the CEMs used in the refurbished F8 sensors differ from those used in the DMSP series F6 - F10 sensors described in Hardy et al.[18] The two overlapping CEM cones of the old design were replaced with a single CEM with a larger collecting cone. This design should more consistently cover the effective particle collecting area behind the exit aperture in the detector.

3. DESCRIPTION OF THE ELECTRON BEAM SYSTEM AND CALIBRATION RESULTS

The electron beam system at the Air Force Geophysics Laboratory in Massachusetts was used to calibrate the SSJ/4 F8 sensors (Marshall et al[19]). The calibration system consists of an illumination system (UV source), a photocathode (quartz substrate coated with a thin film of gold), a high voltage supply system, and gimbal tables. The UV system is configured to provide nearly uniform illumination of the photocathode. The UV light penetrates the gold film generating photoelectrons at the gold-vacuum interface. A negative potential applied to the photocathode sets up an electric field between the photocathode frame and a grounded wire screen in front of the cathode. The photoelectrons are accelerated by this field and pass through the wire screen, forming a nearly monoenergetic, uniform electron beam with about a 15-cm radius. The beam is tunable in energy from approximately 10 V to 50,000 V. The entire system is contained within a set of Helmholtz coils used to cancel out the earth's magnetic field.

The SSJ/4 sensors are calibrated by mounting them on a set of rotational and translational tables so that the angle of the detector's look direction with respect to the beam can be varied. The response of the analyzer is measured vs angle and energy to determine its energy-dependent geometric factor.

---

19. Marshall, F.J., Hardy, D.A., Huber, A., Pantazis, J., McGarity, J., Holeman, E., and Winningham, J.D. (1986) Calibration system for electron detectors in the energy range from 10 eV to 50 keV, Rev. Sci. Instrum., 57(No. 2):229.

The calibration system is computer controlled so that it automatically scans through a two-dimensional array of angles α (azimuth) and β (elevation), relative to the detector aperture for any fixed energy of the incident beam. The counts accumulated as the detector dwells at each angular position are stored on hard disk and later can be transferred to floppy disks or magnetic tape. The current density in the beam is determined by a picoammeter measuring the total photocathode current. The ammeter is held at the negative potential of the photocathode, an arrangement which guards the current monitor from leakage current. This ensures an accurate value of the photocathode beam current that serves as the absolute standard in the calibration.

At the end of each angular scan the computer calculates the energy dependent geometric factor, G(E). By determining G(E) at a series of energies, the response curve for each fixed voltage on the plates can be determined. From the response curve one can determine the channel pass band, ΔE, and by integrating over the response curve one can calculate the energy independent geometric factor, G. G is defined such that

$$j(E) = C/(\Delta T\, G) \qquad (1)$$

where j(E) is the differential flux (electrons/cm^2 sec ster eV) in the channel with central energy E, C is the count level observed in that channel, and ΔT is the accumulation interval for these counts. G is given in units of (cm^2 ster eV). Representative curves for electron channels 2 and 12 of G(E) vs E from this calibration are shown in Figures 3a and 3b, respectively.

Using the electron beam calibration system, the characteristics of the 20 electron channels of the F8 detectors were determined and are listed in Table 1 as follows: the electron energy at the peak of the response curve, E_{peak}, the full width at half maximum of the curve, ΔE, the peak value of the energy-dependent geometric factor, $G(E)_{peak}$, and the energy-integrated geometric factor, G. A total of 126 angular scans was made to map response curves for channels 1, 2, 4, 6, 8 through 13, and 15.

Table 1. Channel Response Characteristics of the SSJ/4 F8 Electron Detector

Channel	E_{peak} (eV)	ΔE (eV)	$G(E)_{peak}$ (cm^2 ster)	G (cm^2 ster eV)
1	31,300	3050	1.70×10^{-4}	5.35×10^{-1}
2	21,100	2000	2.30×10^{-4}	4.60×10^{-1}
3*	14,300	1330	2.65×10^{-4}	3.60×10^{-1}
4	9720	860	3.10×10^{-4}	2.65×10^{-1}
5*	6610	615	3.80×10^{-4}	2.30×10^{-1}
6	4500	430	4.50×10^{-4}	1.85×10^{-1}
7*	3050	284	5.35×10^{-4}	1.50×10^{-1}
8	2070	184	6.70×10^{-4}	1.25×10^{-1}
9	1400	125	7.25×10^{-4}	9.30×10^{-2}
10	950	88	9.05×10^{-4}	7.90×10^{-2}
11	950	85	5.00×10^{-4}	4.40×10^{-2}
12	640	63	5.00×10^{-4}	3.25×10^{-2}
13	440	42	5.00×10^{-4}	2.05×10^{-2}
14*	310	29	5.00×10^{-4}	1.45×10^{-2}
15	210	20	5.00×10^{-4}	1.05×10^{-2}
16*	144	13	5.00×10^{-4}	6.50×10^{-3}
17*	98	9.1	5.00×10^{-4}	4.55×10^{-3}
18*	68	6.3	5.00×10^{-4}	3.15×10^{-3}
19*	45	4.2	5.00×10^{-4}	2.10×10^{-3}
20*	31	2.9	5.00×10^{-4}	1.45×10^{-3}

*Channel response curve not determined by electron beam

$G \Delta E$

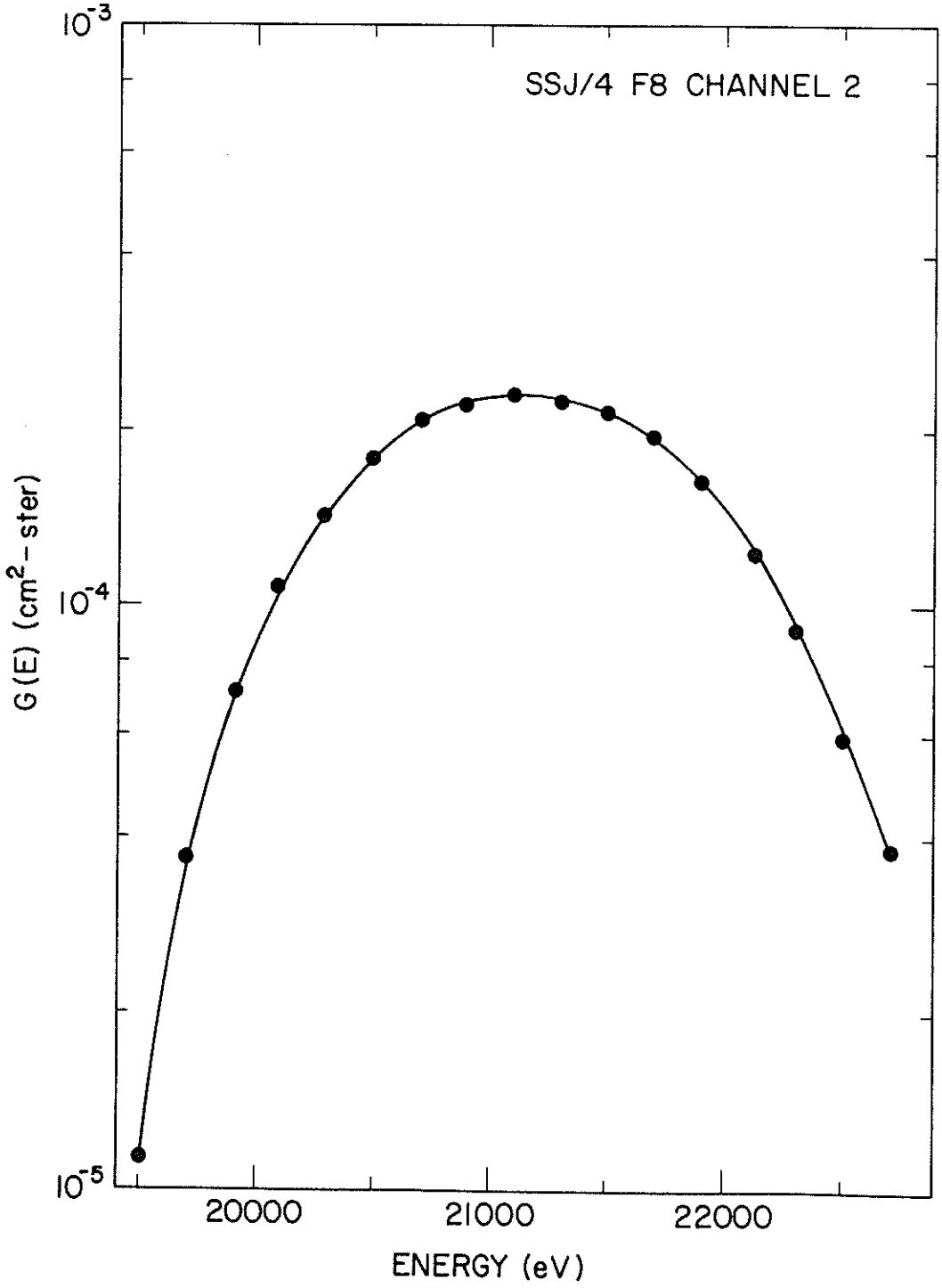

Figure 3a. The Energy-dependent Geometric Factor, G(E), Plotted as a Function of Energy for Channel 2 of the F8 Electron Detector

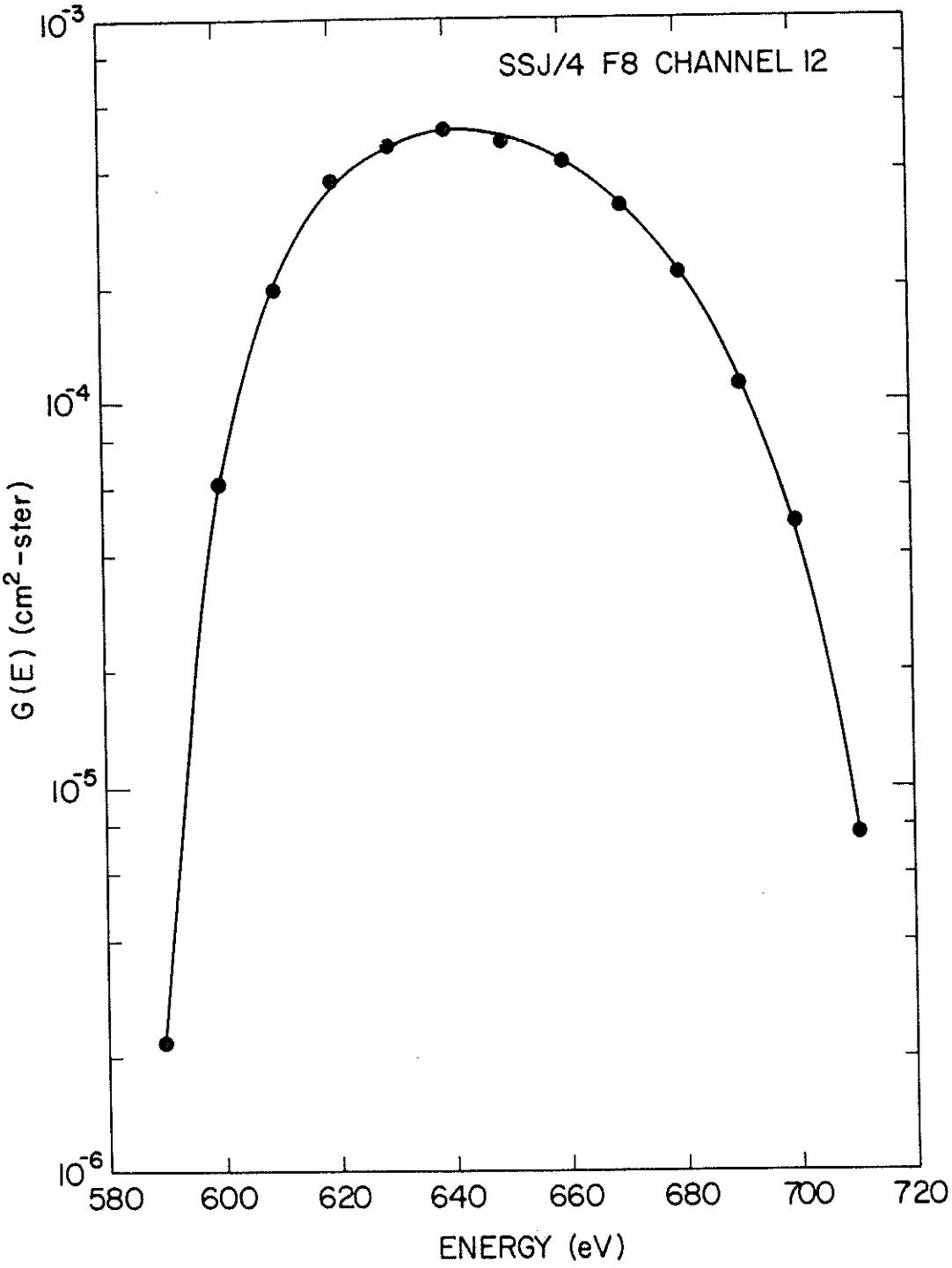

Figure 3b. The Energy-dependent Geometric Factor, G(E), Plotted as a Function of Energy For Channel 12 of the F8 Electron Detector

Due to a time constraint resulting from the instrument delivery deadline coupled with beam distortion effects at low energies, the responses of the remaining channels were not determined experimentally. The beam distortions we attribute to either surface charging or magnetic field inhomogeneities within the beam chamber. The values of these uncalibrated channels (indicated by asterisks) were assigned as follows: the central energies of the low energy sensor were taken from the plate voltages recorded during testing on the ground. Since in the high energy sensor the central energies of the experimentally calibrated channels were consistently higher (by a few percent) than those calculated from the plate potential in the high energy sensor, the central energies for the remaining high energy channels were found by logarithmic interpolation. The values of ΔE for both sensors were calculated from the average $\Delta E/E$ (≈ 9.3 percent) of the channels for which the response curves were determined. The values of $G(E)_{peak}$ for the channels of the high energy sensor were interpolated from the semi-logarithmic plot of $G(E)_{peak}$ vs E shown in Figure 4. All values of $G(E)_{peak}$ for

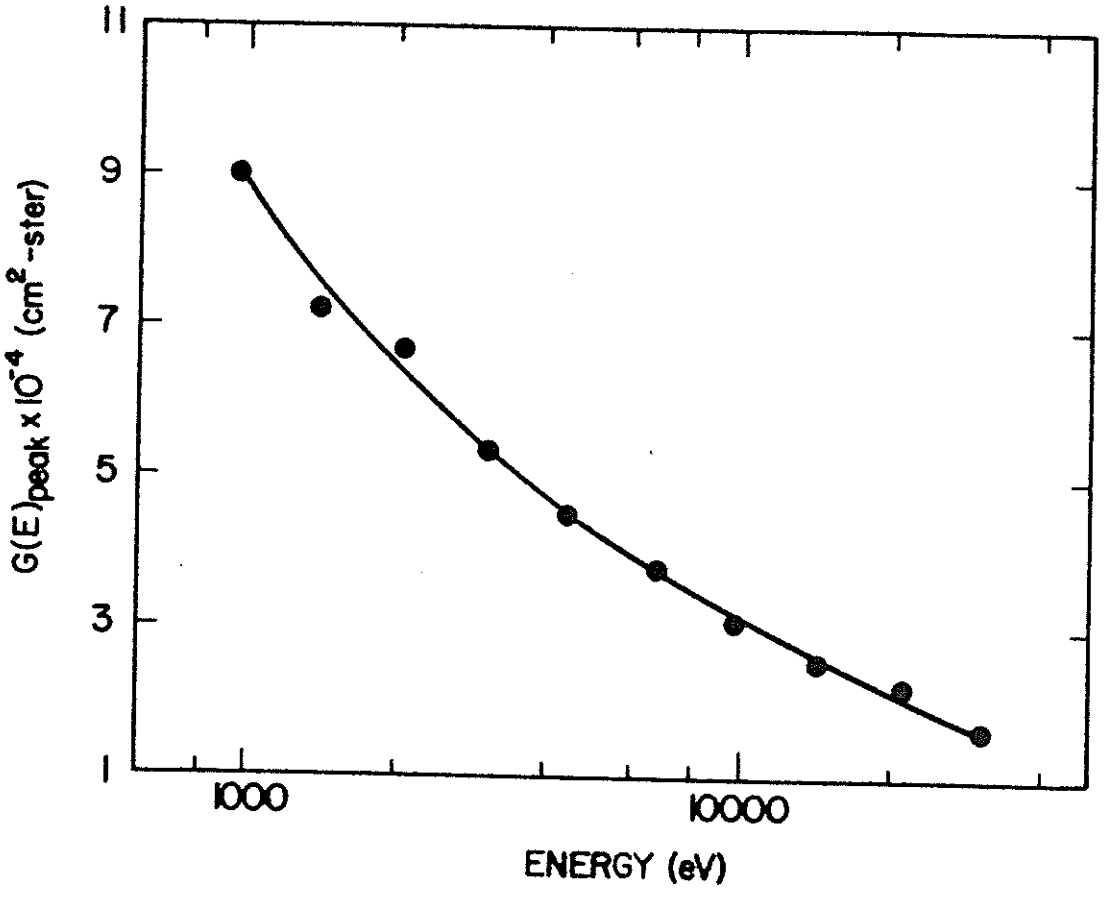

Figure 4. The Peak Energy-dependent Geometric Factor, $G(E)_{peak}$, Plotted as a Function of Energy for the Channels of the High Energy Sensor of the F8 Electron Detector

the channels in the low energy sensor were set equal to the experimentally determined value of channels 11 and 12 [$G(E)_{peak} = 5.0 \times 10^{-4}$ cm^2 ster]. The energy-integrated geometric factors were interpolated or extrapolated from the log-log plots of G vs E shown in Figures 5a and 5b. As expected, all values of the integrated response curves listed in Table 1 differ by no more than a few percent from those calculated using a Gaussian line shape, where $G \approx 1.065 (\Delta E \times G(E))$.

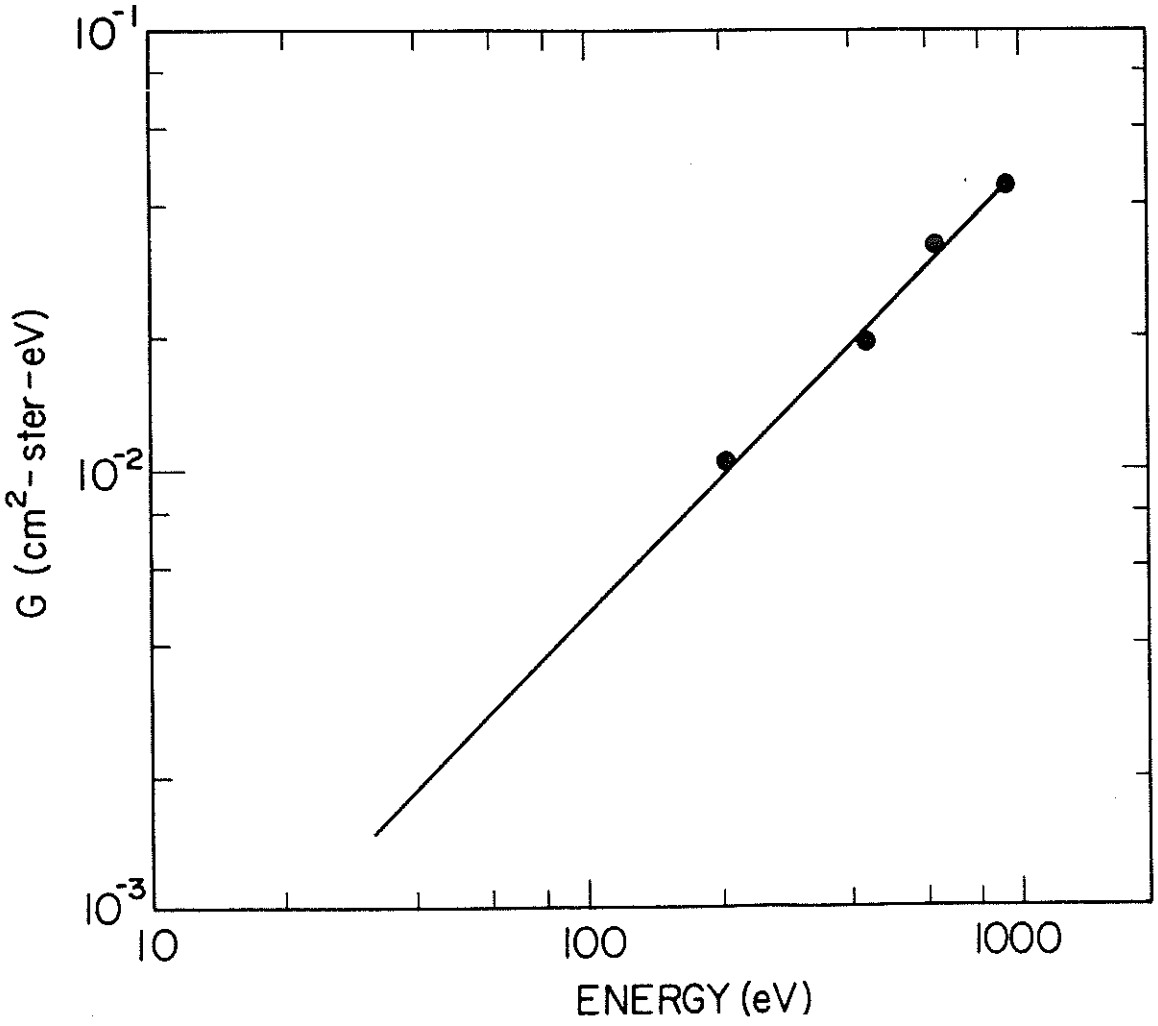

Figure 5a. The Energy-integrated Geometric Factor, G, Plotted as a Function of Energy for the Low Energy Sensor of the F8 Electron Detector

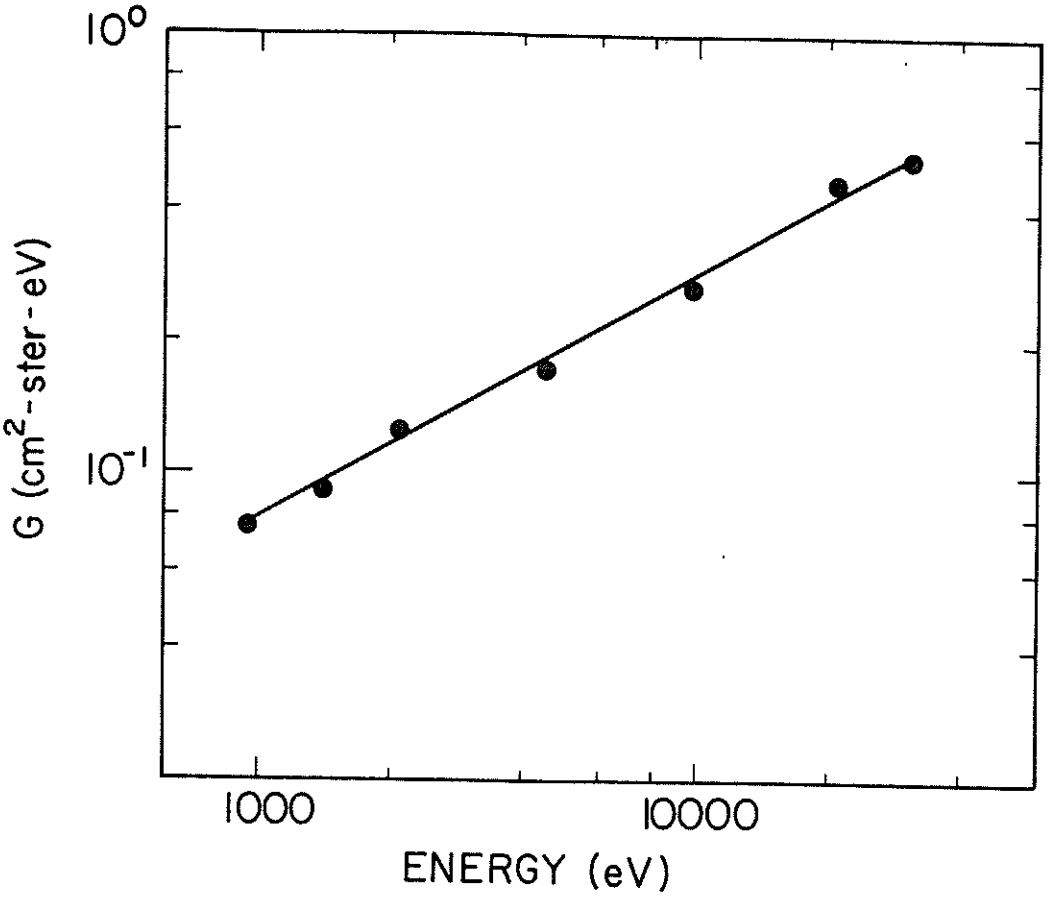

Figure 5b. The Energy-integrated Geometric Factor, G, Plotted as a Function of Energy for the High Energy Sensor of the F8 Electron Detector

The shape of the response curves was the same for all calibrated channels in the high and low energy sensors. This is shown in Figure 6a (6b) where the normalized curves for the channels of the low (high) energy sensor are plotted. The curves were calculated by normalizing the measurements of G(E) for a given channel to $G(E)_{peak}$ observed in that channel and by normalizing the energy, E, at which each measurement was made, to the central energy of the channel, E_{peak}. The decrease in $G(E)_{peak}$ with increasing energy observed in the high energy sensor is attributed exclusively to a change in CEM efficiency. This decrease results from a decrease with increasing energy of the secondary yield of the lead glass from which the CEM is made. Assuming unit efficiency in channel 10 ($E \approx 1$ keV), the CEM efficiencies are determined by the ratio of the $G(E)_{peak}$ in the preceding channels to $G(E)_{peak}$ in channel 10. The values are listed in Table 2.

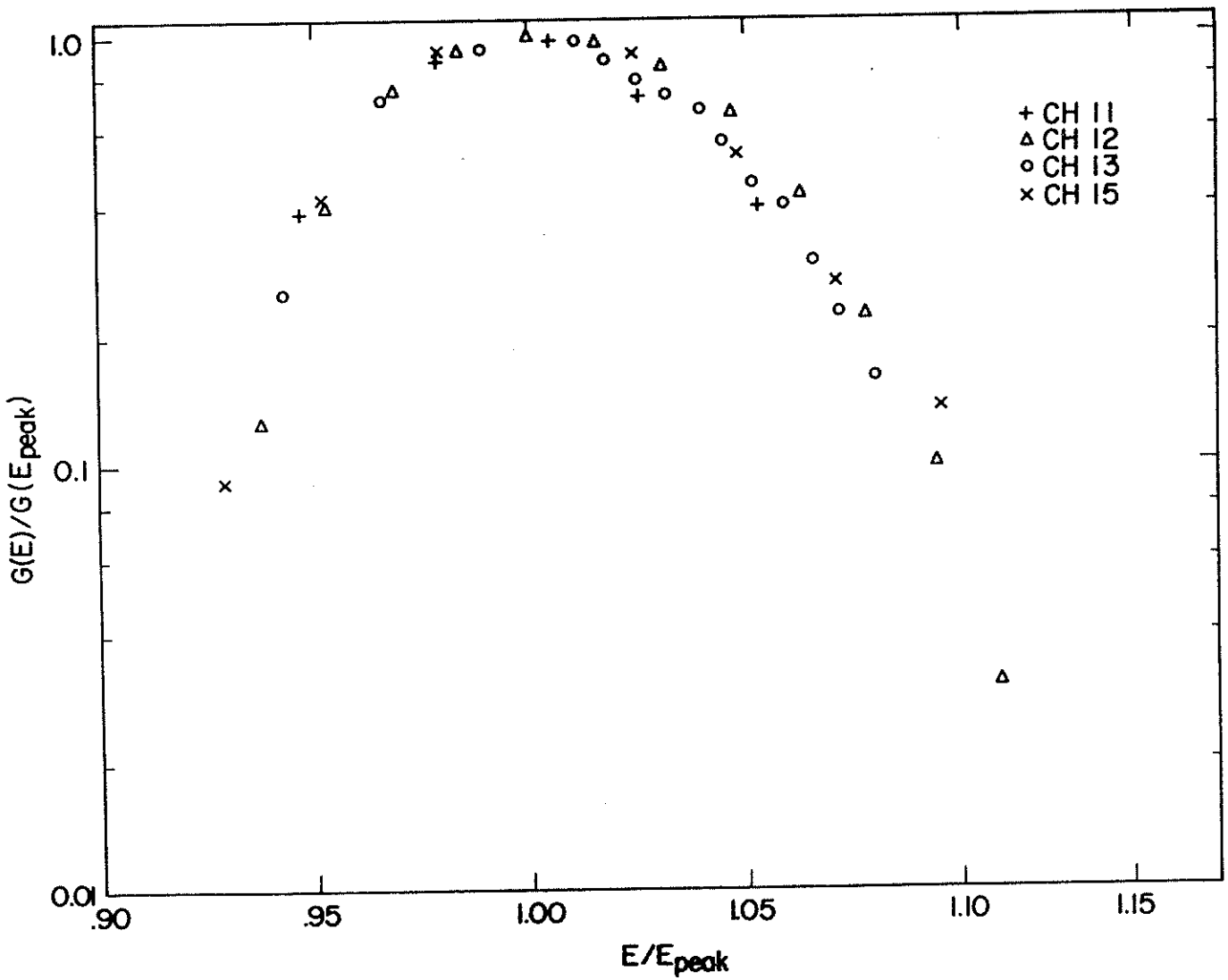

Figure 6a. The Energy-dependent Geometric Factor, G(E), Normalized to the Peak Geometric Factor, $G(E)_{peak}$, Plotted as a Function of Energy, E, Normalized to the Channels' Central Energy, E_{peak}. The figure shows the data from channels 11, 12, 13, and 15 of the low energy sensor of the F8 electron detector

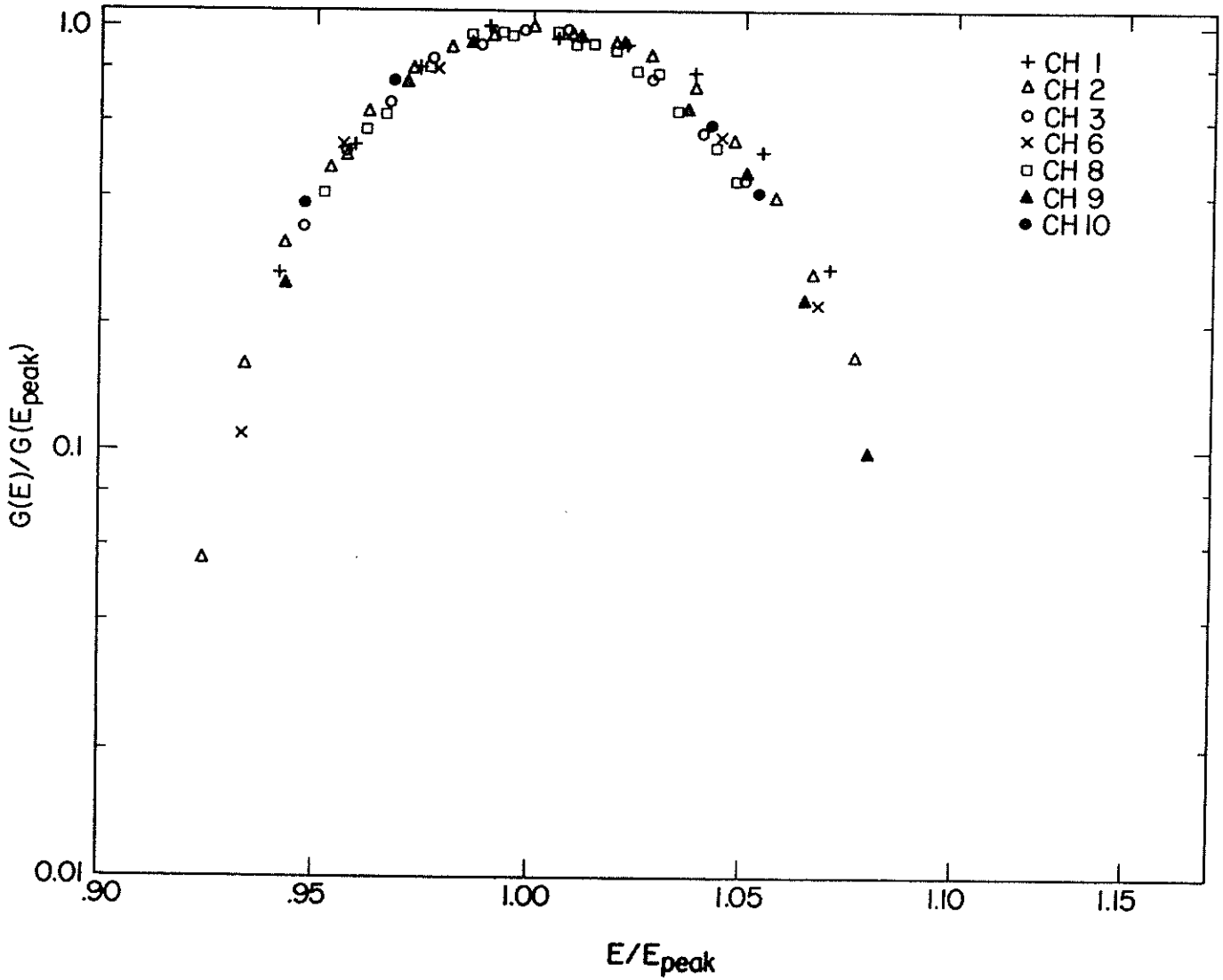

Figure 6b. The Energy-dependent Geometric Factor, G(E), Normalized to the Peak Geometric Factor, $G(E)_{peak}$, Plotted as a Function of Energy, E, Normalized to the Channels' Central Energy, E_{peak}. The figure shows the data from channels 1, 2, 4, 6, 8, 9, and 10 of the high energy sensor of the F8 electron detector

Table 2. CEM Efficiencies of the High Energy Electron Sensor Calculated Assuming Unit Efficiency in Channel 10

Channel	Energy (eV)	Efficiency
1	31,300	0.12
2	21,100	0.25
3	14,300	0.29
4	9720	0.34
5	6610	0.42
6	4500	0.50
7	3050	0.59
8	2070	0.74
9	1400	0.80
10	950	1.00

In order to overcome the low CEM efficiencies at low energies, a post acceleration of 100 V was applied in the low energy sensor. With such a post acceleration, the peak geometric factors for the channels of the low energy sensor should be approximately equal. For channels 13 and 15, however, the values of $G(E)_{peak}$ differed significantly. One possible source of this difference is inhomogeneities in the calibrating beam. As previously mentioned, the beam is produced by illuminating a thin gold surface with a UV lamp. Since neither the illumination nor the thickness of the gold is perfectly uniform, there can be inhomogeneities in the beam intensity. As the beam energy is decreased, the radius of curvature for electrons (in whatever residual field that remains within the Helmholtz coils) also decreases, shifting the orientation of the beam slightly. For the calibration of a specific channel, such a shift can place one of these small inhomogeneities at the entrance aperture of one of the detectors such that an erroneous but reproducible value of G(E) is observed. This may explain the results for channels 13 and 15, where $G(E)_{peak} = 1.04 \times 10^{-3}$ and 2.42×10^{-4} cm^2 ster, respectively. Reasonable values were determined for the central energy and energy width of both channels, but $G(E)_{peak}$ was assumed to be the same as for channels 11 and 12.

Adjustments to the SSJ/4 F8 electron response values were made using in-flight data by a method described in Section 4. The final values are given in Table 4.

The calibration values of the F8 electron detector may be compared to the values listed in Table 2 of Hardy et al.[18] Comparisons of the peak energies and the energy widths show excellent agreement, with the values differing by only a

few percent. There is also good agreement of the peak geometric factors and the energy-integrated geometric factors of the high energy sensors, with differences averaging 11 percent and 14 percent, respectively. In the low energy sensors, however, the values of $G(E)_{peak}$ and G of the F8 detector are a factor of 2 to 5 greater than those from Table 2. The significant difference we attribute to the use of the new CEMs within the refurbished detector. We believe that the larger channeltron collecting cones more completely cover the detector's effective collecting area.

The angular acceptance of the F8 detector was determined from the response of channels 10 and 11 at approximately their central energies in directions perpendicular and parallel to the two cylindrical plates of the analyzer. The angle α is measured within the plane of the plates' radii of curvature; and the angle β is measured perpendicular to the plate's radii of curvature. The two angles are shown in Figure 2 and the response curves in both angles are shown in Figure 7. The response curves are normalized to the counts observed where $\alpha = \beta = 0°$. $\Delta\alpha$ and $\Delta\beta$ are defined as the full width half maximum of the angular response. While $\Delta\beta$ is defined primarily from aperture geometry, $\Delta\alpha$ is both electrostatically and geometrically defined since α is measured in the plane of the electric field direction between the cylindrical detector plates. The values for $\Delta\alpha$ and $\Delta\beta$ for the F8 detector are given in Table 3a and are compared to those found for the F10 detector. The results differ by less than 20 percent.

The values of the angular response for the remaining electron channels of the F8 detector's high energy sensor are nearly identical to those of channel 10. At low energies the angular response broadens. We attribute this to the energy width of the calibration beam in the direction perpendicular to the acceleration and possibly to surface charging effects within the vacuum chamber. The values of $\Delta\alpha$ and $\Delta\beta$ for channels 11, 12, 13, and 15 of the F8 detector are given in Table 3b. This effect will be discussed in more detail in Section 6.

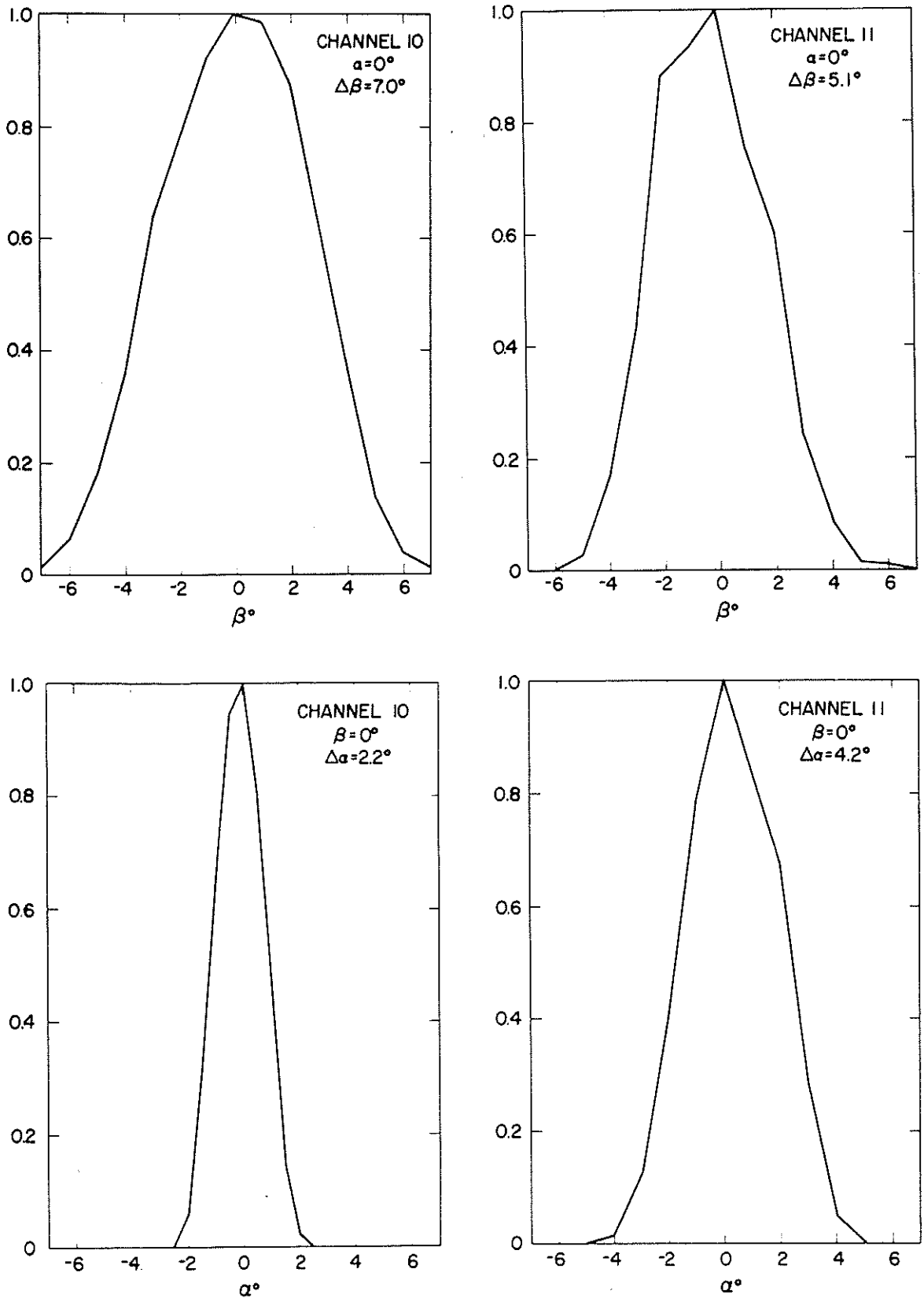

Figure 7. Angular Response of Electron Channels 10 and 11 for the SSJ/4 F8 Detector. The top curves show the normalized response for the angle α with $\beta = 0°$. The bottom curves show the variation in β with $\alpha = 0°$

Table 3a. The Full Width Half Maximum Angular Response, $\Delta\alpha$ and $\Delta\beta$, for the SSJ/4 F8 and F10 Electron Detectors, Channels 10 and 11

Channel 10			Channel 11		
	$\Delta\alpha$	$\Delta\beta$		$\Delta\alpha$	$\Delta\beta$
F10	2.05°	8.4°	F10	3.6°	4.5°
F8	2.2°	7.0°	F8	4.2°	5.1°

Table 3b. The Full Width Half Maximum Angular Response, $\Delta\alpha$ and $\Delta\beta$, for Channels 11, 12, 13, and 15 of the Low Energy Electron Sensor of the SSJ/4 F8 Detector

Channel	$\Delta\alpha$	$\Delta\beta$
11	4.2°	5.1°
12	4.0°	4.8°
13	4.8°	5.4°
15	5.9°	7.2°

4. ION GEOMETRIC FACTORS AND ADJUSTED ELECTRON GEOMETRIC FACTORS

In-flight data were used to adjust the values of the electron geometric factors and a combination of electron calibration results and in-flight data were used to assign ion geometric factors. Analysis of electron data from auroral passes of the F8 satellite showed that using the initially assigned geometric factors the differential electron flux measured by channels 10 and 11 at 950 eV differed, with channel 10 consistently observing a lower flux than channel 11. In flight these two channels should record counts proportional to the ratio of their respective G_{peak} values times the full energy width at half maximum:

$$CNTS_{10}/CNTS_{11} = (G_{peak})_{10}\Delta E_{10}/(G_{peak})_{11}\Delta E_{11} = \text{constant} \ . \qquad (2)$$

Since the ΔEs have already been specified and G_{peak} for the high energy sensor has been determined with more certainty than for the low energy sensor, G_{peak} for channel 11 can be adjusted by using Eq. (2).

Electron data in the diffuse auroral region where the count levels are typically greater than 100 in the low energy detector were used to calculate the count ratio. Data were chosen from 25 to 31 June 1987 and were averaged over 1-min time intervals. A total of 269 1-min intervals was used to calculate F8 electron ratios, the average ratio being approximately 1.3. The G_{peak} of 7.10×10^{-4} cm^2 ster determined from this average ratio was applied for all low energy channels since their efficiency is taken as unity. Using the known shape of the response curves the integrated geometric factors were redetermined. The results are shown in Table 4. Subsequent calibration on another SSJ/4 detector verified that the value of 7.10×10^{-4} cm^2 ster is correct.

To assign the characteristics for the high energy ion channels we used two assumptions. First, since the high energy electron and ion sensors are identical except for the change in plate polarity, their 950 eV channels should have the same peak geometric factor and shape. Second, the efficiency of the ion CEM should be unity at all energies at and above 950 eV. These two assumptions imply that the peak geometric factor of all the high energy ion channels is 9.05×10^{-4} cm^2 ster, and the channel widths are identical to those of the high energy electron sensor. The integrated ion geometric factors were then calculated using these energy widths and peak geometric factor.

Assigning the response characteristics to the low energy ion sensor was very similar to the procedure used to adjust the low energy electron sensor characteristics described earlier in this section. First, ΔE/E was determined by the calibration of an SSJ/4 prototype ion detector (see Section 7). ΔE/E was found to be approximately 16 percent. The wider channel band is due to the larger opening aperture of the low energy ion sensor. Second, using in-flight ion data, the ratio of ion counts in channel 11 to channel 10 was found to be approximately 26.2. Inserting these values into Eq. (2), we then found the peak geometric factor for all channels of the low energy ion sensor to be 1.50×10^{-2} cm^2 ster. The ion channel response characteristics are listed in Table 5. The SSJ/4 F8 ion geometric factors are in very good agreement with those derived for the F6 and F8 detectors (see Table 4 of Hardy et al[18]).

Table 4. Adjusted Channel Response Characteristics of the SSJ/4 F8 Electron Detector

Channel	E_{peak} (eV)	ΔE (eV)	$G(E)_{peak}$ (cm^2 ster)	G (cm^2 ster eV)
1	31,300	3050	1.70×10^{-4}	5.35×10^{-1}
2	21,100	2000	2.30×10^{-4}	4.60×10^{-1}
3*	14,300	1330	2.65×10^{-4}	3.60×10^{-1}
4	9720	860	3.10×10^{-4}	2.65×10^{-1}
5*	6610	615	3.80×10^{-4}	2.30×10^{-1}
6	4500	430	4.50×10^{-4}	1.85×10^{-1}
7*	3050	284	5.35×10^{-4}	1.50×10^{-1}
8	2070	184	6.70×10^{-4}	1.25×10^{-1}
9	1400	125	7.25×10^{-4}	9.30×10^{-2}
10	950	88	9.05×10^{-4}	7.90×10^{-2}
11	950	85	7.10×10^{-4}	5.60×10^{-2}
12	640	63	7.10×10^{-4}	4.15×10^{-2}
13	440	42	7.10×10^{-4}	2.60×10^{-2}
14*	310	29	7.10×10^{-4}	1.85×10^{-2}
15	210	20	7.10×10^{-4}	1.35×10^{-2}
16*	144	13	7.10×10^{-4}	8.30×10^{-3}
17*	98	9.1	7.10×10^{-4}	5.80×10^{-3}
18*	68	6.3	7.10×10^{-4}	4.00×10^{-3}
19*	45	4.2	7.10×10^{-4}	2.70×10^{-3}
20*	31	2.9	7.10×10^{-4}	1.85×10^{-3}

*Channel response curve not determined by electron beam

$1.70 \times 10^{-4} \times \Delta E$

$1.70 \times 10^{-4} \times E \times \Omega$

$\sim 10\%$

$G = G_E(E)_{peak} \times \Delta E$

Table 5. Channel Response Characteristics of the SSJ/4 F8 Ion Detector

Channel	E_{peak} (eV)	ΔE (eV)	$G(E)_{peak}$ (cm^2 ster)	G (cm^2 ster eV)
1	31,300	3050	9.05×10^{-4}	2.75×10^{-0}
2	21,100	2000	9.05×10^{-4}	1.80×10^{-0}
3	14,300	1330	9.05×10^{-4}	1.20×10^{-0}
4	9720	860	9.05×10^{-4}	7.80×10^{-1}
5	6610	615	9.05×10^{-4}	5.55×10^{-1}
6	4500	430	9.05×10^{-4}	3.90×10^{-1}
7	3050	284	9.05×10^{-4}	2.55×10^{-1}
8	2070	184	9.05×10^{-4}	1.65×10^{-1}
9	1400	125	9.05×10^{-4}	1.15×10^{-1}
10	950	88	9.05×10^{-4}	7.90×10^{-2}
11	950	152	1.50×10^{-2}	2.30×10^{-0}
12	640	102	1.50×10^{-2}	1.55×10^{-0}
13	440	70	1.50×10^{-2}	1.05×10^{-0}
14	310	50	1.50×10^{-2}	7.50×10^{-1}
15	210	34	1.50×10^{-2}	5.10×10^{-1}
16	144	23	1.50×10^{-2}	3.45×10^{-1}
17	98	16	1.50×10^{-2}	2.40×10^{-1}
18	68	11	1.50×10^{-2}	1.65×10^{-1}
19	45	7.2	1.50×10^{-2}	1.10×10^{-1}
20	31	5.0	1.50×10^{-2}	7.50×10^{-2}

$$G = G(E)_{peak} \times \Delta E$$

The particle counts from the SSJ/4 detectors can be converted to differential flux by using the geometric factors listed in Tables 4 and 5 and the equation

$$J(E_i) = C_i/[\Delta T\, G_i] \quad , \tag{3}$$

where C_i is the number of counts detected by the CEM with central energy E_i, ΔT is the accumulation time, equal to 98 msec, and G_i is the energy integrated geometric factor for channel i in cm^2 ster eV.

5. CORRECTION FOR ELECTRON CONTAMINATION IN THE F8 ION AND ELECTRON DETECTORS

Since the auroral ion flux is typically a factor of 10 to 100 less than that for electrons, we maximized the areas of the front and back ion apertures in order to enlarge the ion geometric factor. While this produced the desired result of increased sensitivity, it also left the ion detector susceptible to some small contamination from electrons scattering through the plates and being counted. Studies of energetic electron scattering through the plates of an electrostatic analyzer have not been found in the literature. To quantify the effects of electron scattering, the ion channels' angular response to electrons with energies between 1 and 40 keV was measured to determine their energy-dependent geometric factor, $G_i(E_e)$, to electrons. The channel response, $G_e(E_e)$, of the electron detector to high energy electrons was also determined.

As an example of the data used to determine the electron rejection within the SSJ/4 detector, the angular response of electron and ion channel 2 to a 10-keV electron beam is shown in Figures 8a and 8b, respectively, as three-dimensional plots of counts vs azimuthal angle α, and elevation angle, β. The data shown are from a later calibration of the SSJ/4 F12 detector (identical to the F8 detector). Although the gross results of the electron rejection experiments for both sets of detectors were the same, a longer accumulation interval for the F12 detector resulted in better counting statistics. Counts were accumulated in 10-sec intervals in 2° steps as the detector swept an angular area 50° azimuthally by 70° in elevation. The look-direction of the detector was aligned antiparallel to the beam at the point (α = 18°, β = 10°). The count level is seen to maximize asymmetrically for look-directions of the detector displaced approximately ± 10° in elevation from the beam direction. The maximum count level occurs at negative elevation angles for electrons and positive angles for ions; a phenomenon probably resulting from opposite deflection biasing of the plates for electrons and ions.

The angular displacement of the peak counts from the beam direction increases with decreasing plate voltage.

The experimental results of $G_i(E_e)$ for six channels of the low (high) energy sensor of the F8 ion detector are plotted vs electron beam energy in Figure 9a (9b). The smooth curves shown in both figures are drawn to approximate the electron rejection curve for the 12 ion channels. The curves show that the values of $G_i(E_e)$ increase with increasing energy above 1 keV; approaching a constant value at high energy. Since a smaller electric field between the plates makes it easier for the electrons to scatter through the plates, the electron contamination is greatest in the lowest energy channels of both ion sensors, (that is, $G_i(E_e)$ is larger for channel 20 than channel 11, and larger for channel 10 than channel 1). The high energy ion sensor is less sensitive by a factor of 5 to 10 than the low energy sensor to electron contamination. A complete set of $G_i(E_e)$ values for all energy channels of the SSJ/4 F8 ion detector, obtained by means of linear interpolation from the electron curves shown in Figures 9a and 9b, is given in Table 6.

Electron rejection values for the SSJ/4 F10 ion detector were determined over the same energy range as the F8 detector (see Figures 16 and 17 and Table 5 of Hardy et al[18]). Comparisons between the values of $G_i(E_e)$ of the low energy sensor show that for a given channel and electron beam energy, $G_i(E_e)$ of the F8 detector is at least a factor of 2 less than $G_i(E_e)$ of the F10 detector; the difference increasing with decreasing beam energy. The rejection values of the F10 high energy sensor were too scattered to be fitted with a smooth rejection curve. Even so, the range of $G_i(E_e)$ values of the F10 high energy sensor bounded by $G_i(E_e)_{max}$ and $G_i(E_e)_{min}$ curves encompasses only about half of the $G_i(E_e)$ values of the F8 detector, with the remaining values, particularly at beam energies less than 4 keV, falling below this range. These differences are again attributed to the change in CEM design.

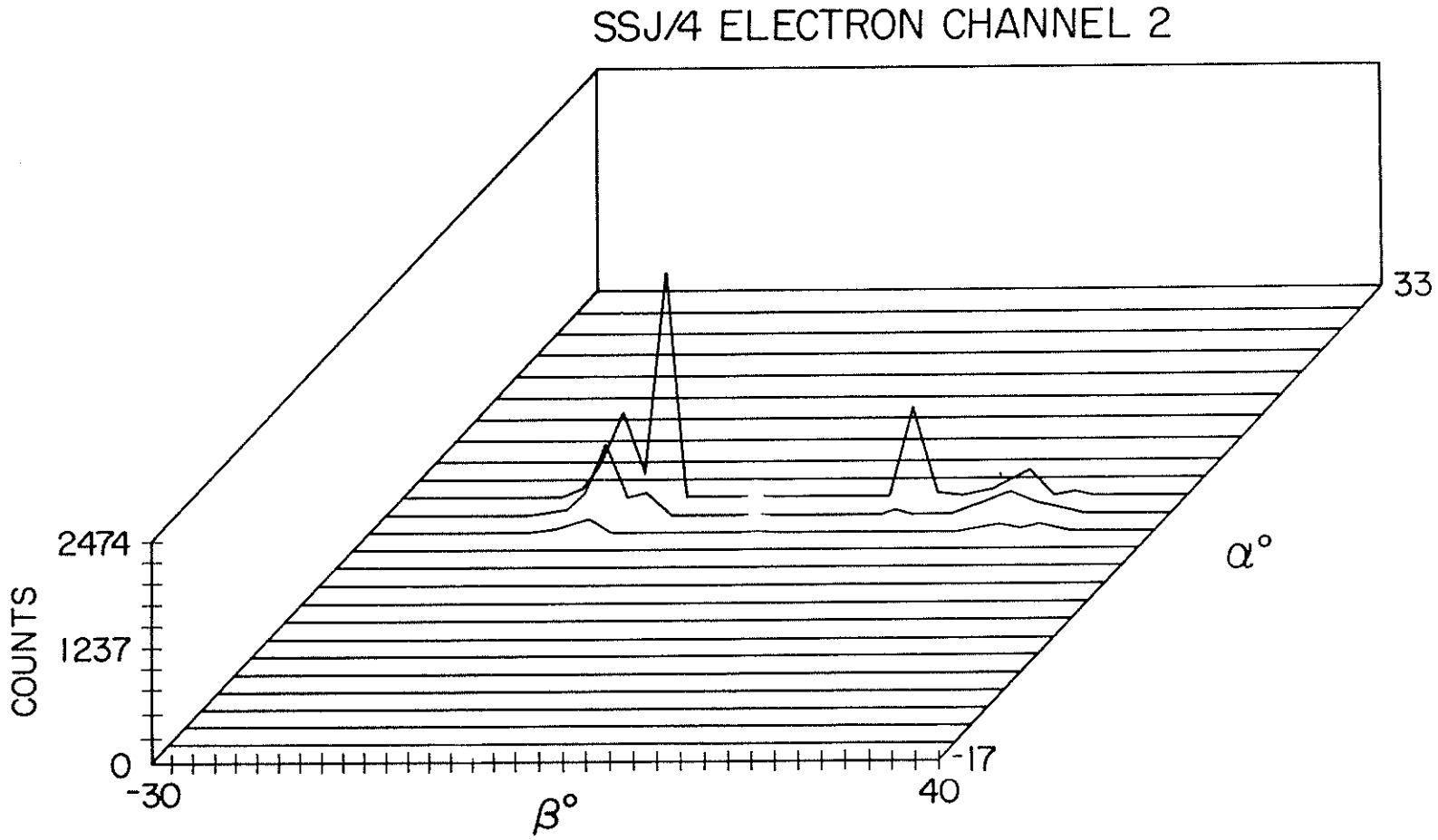

Figure 8a. The Wide Angle Response of Electron Channel 2 to a 10 keV Electron Beam. Electron counts per 10-sec accumulation interval are plotted vs azimuthal angle α and elevation angle β. The data shown are from a later calibration of the SSJ/4 F12 detector set

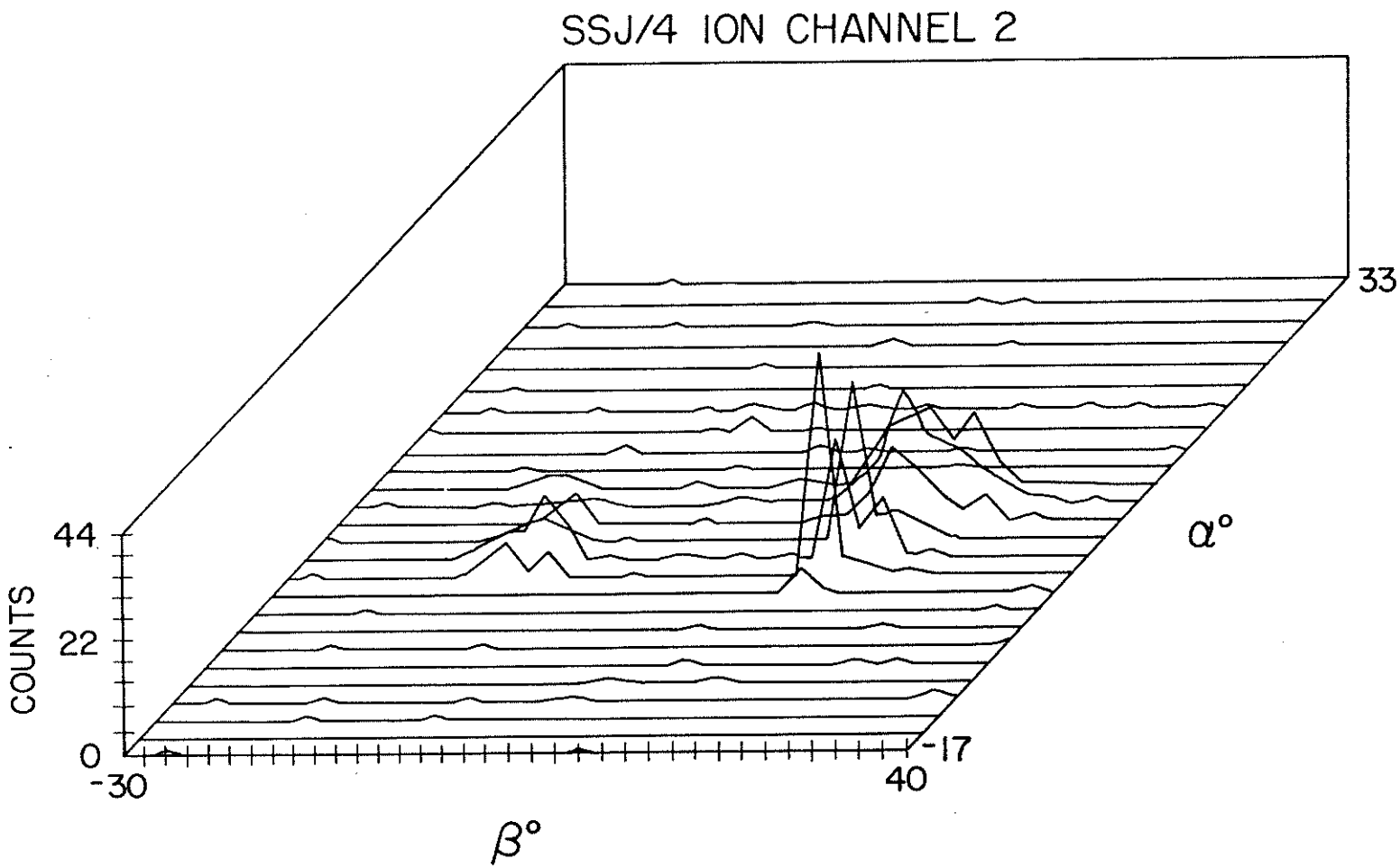

Figure 8b. The Wide Angle Response of Ion Channel 2 to a 10-keV Electron Beam. Electron counts per 1-sec accumulation interval are plotted vs azimuthal angle α and elevation angle β. The data shown are from a later calibration of the SSJ/4 F12 detector set

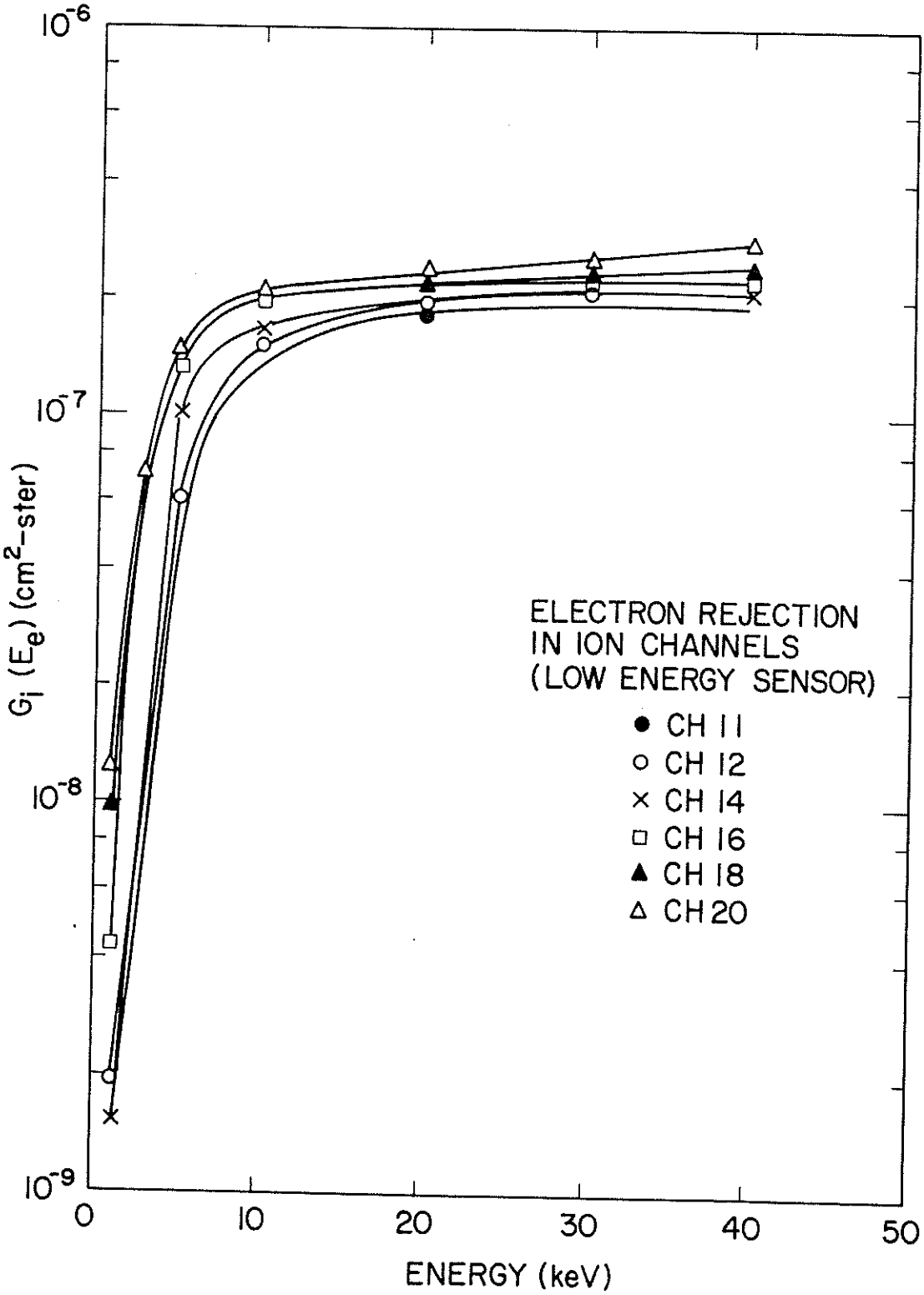

Figure 9a. The Energy-dependent Geometric Factors, $G_i(E_e)$, for the Ion Channels' Response to the Electron Contaminants in the Low Energy Sensor Plotted vs Electron Beam Energy. Data were taken for ion channels 11, 12, 14, 16, 18, and 20 of the SSJ/4 F8 detector. The six solid lines give an approximate fit to the measurements in each channel

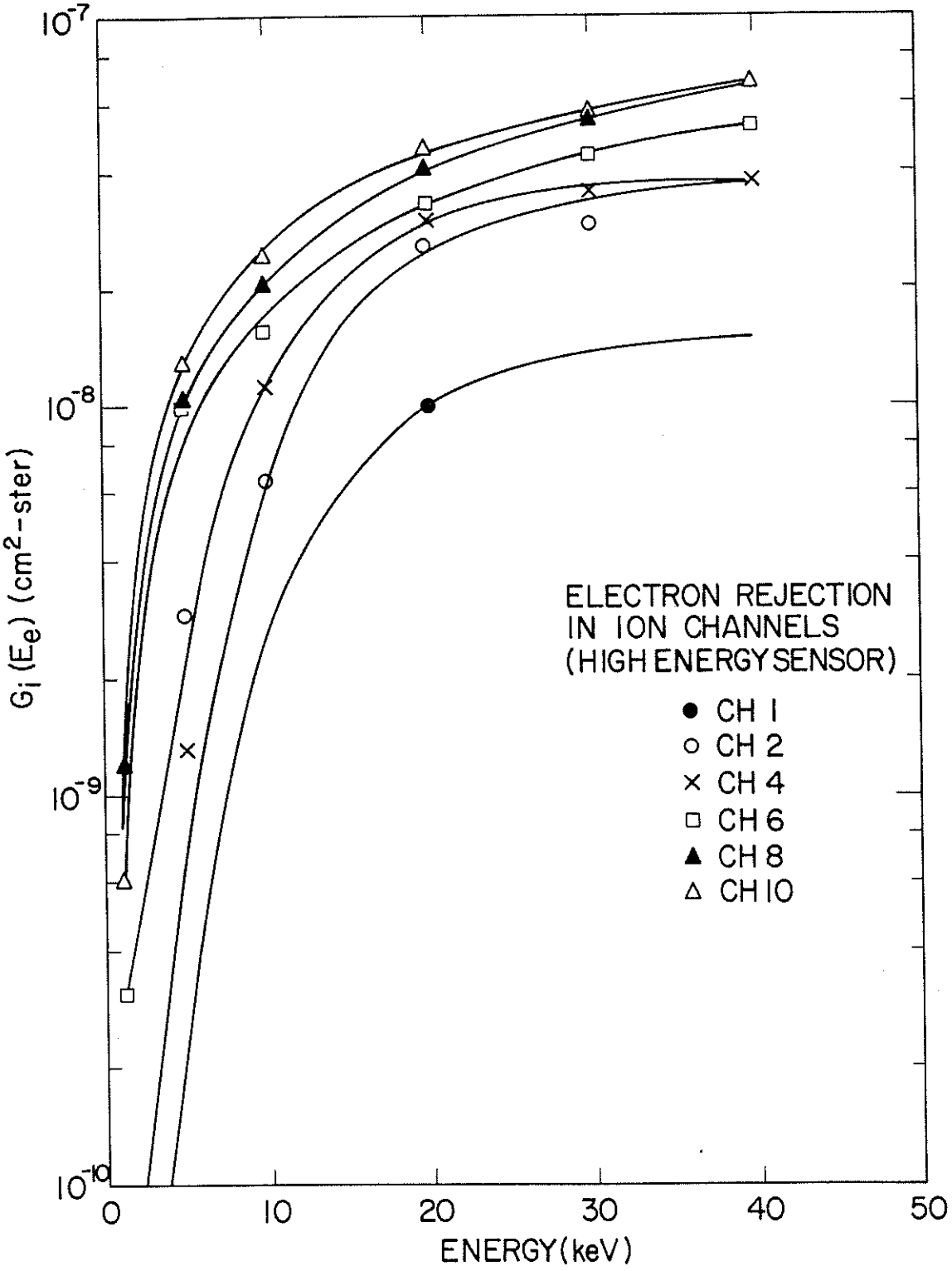

Figure 9b. The Energy-dependent Geometric Factors, $G_i(E_e)$, for the Ion Channels' Response to the Electron Contaminants in the High Energy Sensor Plotted vs Electron Beam Energy. Data were taken for ion channels 1, 2, 4, 6, 8, and 10 of the SSJ/4 F8 detector. The six solid lines give an approximate fit to the measurements in each channel

Table 6. Electron Rejection Curve Values for the SSJ/4 F8 Ion Detector

	$G_i(E_e)$ cm^2 ster (High Energy Sensor)										
	E_e(eV)	Ch1	Ch2	Ch 3	Ch 4	Ch 5	Ch 6	Ch 7	Ch 8	Ch 9	Ch 10
(1)	31,300	1.4(-8)	3.4(-8)	3.5(-8)	3.6(-8)	4.1(-8)	4.6(-8)	5.1(-8)	5.6(-8)	5.8(-8)	6.0(-8)
(2)	21,100	1.0(-8)	2.6(-8)	2.8(-8)	3.1(-8)	3.2(-8)	3.4(-8)	3.8(-8)	4.2(-8)	4.4(-8)	4.6(-8)
(3)	14,300	6.0(-9)	1.5(-8)	1.7(-8)	2.0(-8)	2.1(-8)	2.3(-8)	2.6(-8)	2.9(-8)	3.1(-8)	3.4(-8)
(4)	9720	2.6(-9)	6.4(-9)	8.4(-9)	1.1(-8)	1.4(-8)	1.7(-8)	1.8(-8)	2.0(-8)	2.2(-8)	2.4(-8)
(5)	6610	7.6(-10)	1.9(-9)	2.8(-9)	4.2(-9)	7.1(-9)	1.2(-8)	1.3(-8)	1.4(-8)	1.5(-8)	1.7(-8)
(6)	4500	1.9(-10)	4.8(-10)	8.8(-10)	1.6(-9)	3.5(-9)	7.6(-9)	8.0(-9)	8.4(-9)	9.6(-9)	1.1(-8)
(7)	3050	8.4(-11)	2.1(-10)	4.1(-10)	8.2(-10)	2.1(-9)	5.2(-9)	5.2(-9)	5.2(-9)	5.9(-9)	6.8(-9)
(8)	2070	4.0(-11)	1.1(-10)	2.1(-10)	4.6(-10)	1.0(-9)	2.3(-9)	2.4(-9)	2.6(-9)	3.0(-9)	3.4(-9)
(9)	1400	0	0	1.9(-10)	3.5(-10)	4.5(-10)	5.8(-10)	8.7(-10)	1.3(-9)	1.6(-9)	1.9(-9)
(10)	950	0	0	1.8(-10)	3.2(-10)	3.2(-10)	3.2(-10)	5.2(-10)	8.6(-10)	8.6(-10)	8.6(-10)
	$G_i(E_e)$ cm^2 ster (Low Energy Sensor)										
	E_e(eV)	Ch 11	Ch 12	Ch 13	Ch 14	Ch 15	Ch 16	Ch 17	Ch 18	Ch 19	Ch 20
(1)	31,300	1.9(-7)	2.1(-7)	2.1(-7)	2.1(-7)	2.1(-7)	2.2(-7)	2.2(-7)	2.3(-7)	2.4(-7)	2.6(-7)
(2)	21,100	1.9(-7)	2.1(-7)	2.1(-7)	2.1(-7)	2.1(-7)	2.1(-7)	2.1(-7)	2.2(-7)	2.2(-7)	2.3(-7)
(3)	14,300	1.6(-7)	1.8(-7)	1.8(-7)	1.9(-7)	2.0(-7)	2.1(-7)	2.1(-7)	2.1(-7)	2.1(-7)	2.2(-7)
(4)	9720	1.4(-7)	1.5(-7)	1.6(-7)	1.7(-7)	1.8(-7)	2.0(-7)	2.0(-7)	2.1(-7)	2.1(-7)	2.1(-7)
(5)	6610	9.0(-8)	1.0(-7)	1.1(-7)	1.3(-7)	1.5(-7)	1.7(-7)	1.7(-7)	1.8(-7)	1.8(-7)	1.8(-7)
(6)	4500	3.2(-8)	3.6(-8)	4.5(-8)	5.6(-8)	8.2(-8)	1.2(-7)	1.2(-7)	1.3(-7)	1.3(-7)	1.3(-7)
(7)	3050	9.0(-9)	1.0(-8)	1.1(-8)	1.3(-8)	2.8(-8)	6.0(-8)	6.6(-8)	7.2(-8)	7.2(-8)	7.2(-8)
(8)	2070	4.0(-9)	4.4(-9)	4.6(-9)	4.8(-9)	1.1(-8)	2.4(-8)	2.9(-8)	3.6(-8)	3.6(-8)	3.6(-8)
(9)	1400	2.0(-9)	2.2(-9)	2.2(-9)	2.2(-9)	4.2(-9)	8.0(-9)	1.1(-8)	1.5(-8)	1.6(-8)	1.7(-8)
(10)	950	1.5(-9)	1.7(-9)	1.7(-9)	1.7(-9)	2.7(-9)	4.4(-9)	6.6(-9)	9.8(-9)	1.1(-8)	1.2(-8)

Note: 1.4(-8) = 1.4×10^{-8} and so on

The full response curves for the high energy electron channels 2, 4, 6, 8, and 10 are shown in Figure 10. $G_e(E_e)$ includes only those values outside the response curve's central energy bandwidth. The response curves are seen to fall more steeply at energies below the peak than above. The high energy tails approach values of 7 $(\pm 3) \times 10^{-8}$ cm^2 ster, more than 3 orders of magnitude less than the values of the peak geometric factors.

The response of the low energy electron sensor to high energy electrons is very nearly constant, as shown in Figure 10b. Like the ion channels, the contamination from energetic electrons is greatest in the lowest energy channels of the electron detector (that is, $G_e(E_e)$ is larger for channel 20 than for channel 12, 2.2×10^{-7} vs 1.3×10^{-7} cm^2 ster, respectively).

The rejection curve values listed in Tables 6 and 7 can be used to calculate the counts contributed by the electrons that scatter through the ith channel of the ion/electron detector from the following equation:

$$C_{RJ}(\text{counts/sec}) = \int J(E)\, G(E)\, dE \ ;$$

$$C_{RJ} \approx J(E_1) G_i(E_1) (E_1 - E_2) + \sum_{j=2}^{9} J(E_j) G_i(E_j) (E_{j-1} - E_{j+1})/2 + J(E_{10}) G_i(E_{10}) (E_9 - E_{10}) \ , \qquad (4)$$

where $J(E_j)$ is the differential number flux of precipitating electrons of energy, E_j, measured by the SSJ/4 detector, and $G_i(E_j)$ is the energy dependent geometric factor for the ith ion/electron channel to electrons of energy E_j. Equation (4) should give a good estimate of rejected counts (that is, C_{RJ}) as long as the major portion of the electron spectrum is within the energy range covered by the SSJ/4 detector. The real count rate in each channel is found by subtracting C_{RJ} from the measured count rate. For electron contamination of the ion channel, Eq. (4) is exact. For electron contamination of the electron channels, Eq. (4) is a good approximation so long as the correction does not lower the differential flux in channels contributing significantly to the scattering.

In the DMSP orbit, the correction for electron scattering ranges from insignificant to being so large as to obscure all real ion counts and low energy electron counts. The correction depends on the spectral shape of both electrons and ions and is not easily categorized. However, corrections for electron contamination must be made in intense electron events, such as inverted-Vs in the polar cap and boundary plasma sheet regions. For diffuse aurora the correction is in the neighborhood of ten percent.

Note: 1.4(-8) = 1.4×10^{-8} and so on

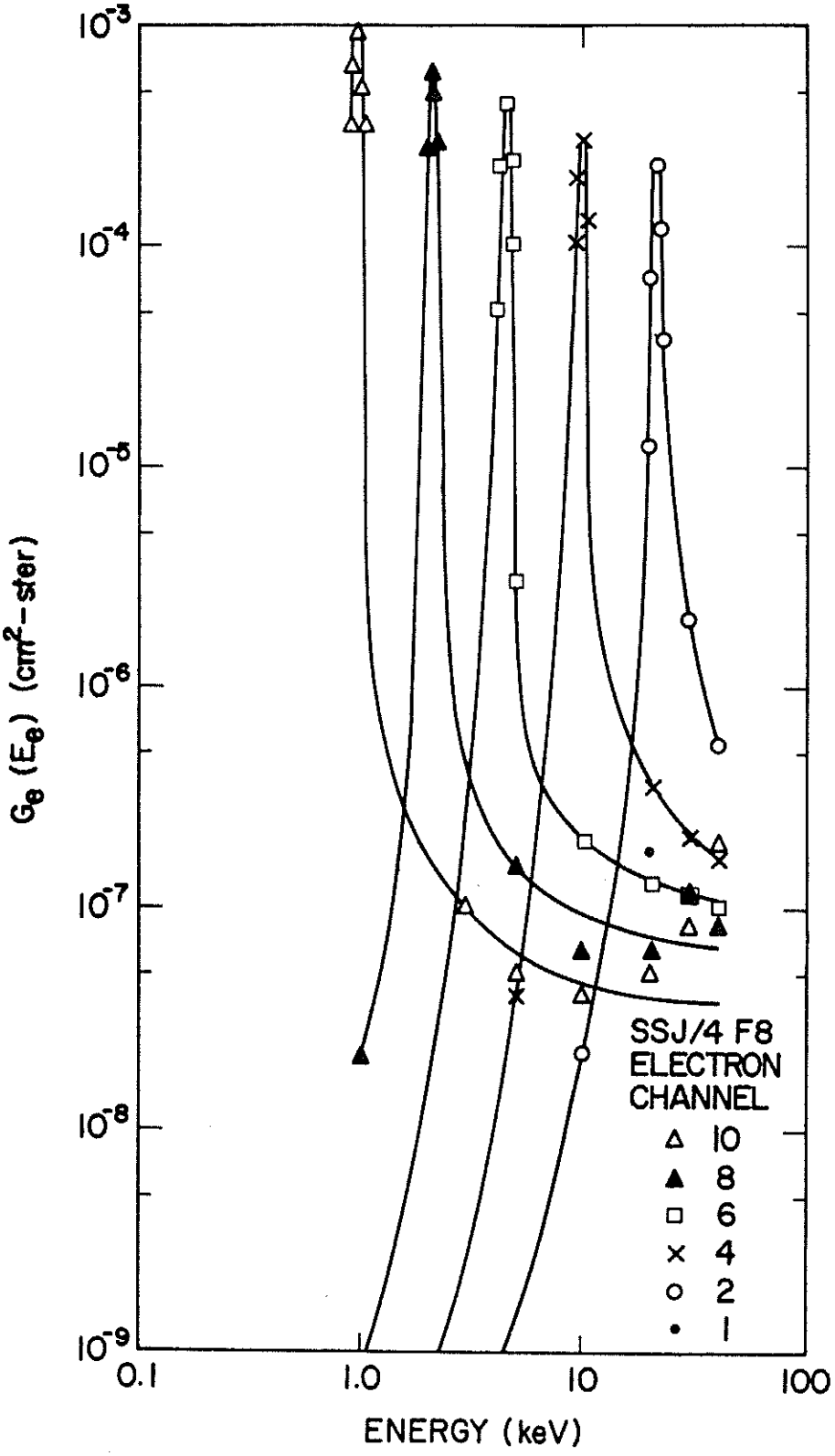

Figure 10a. The Channel Response, $G_e(E_e)$, of the High Energy Electron Sensor to Electron Beam Energies Between 1 and 40 keV. Data were taken for channels 1, 2, 4, 6, 8, and 10 of the SSJ/4 F8 detector

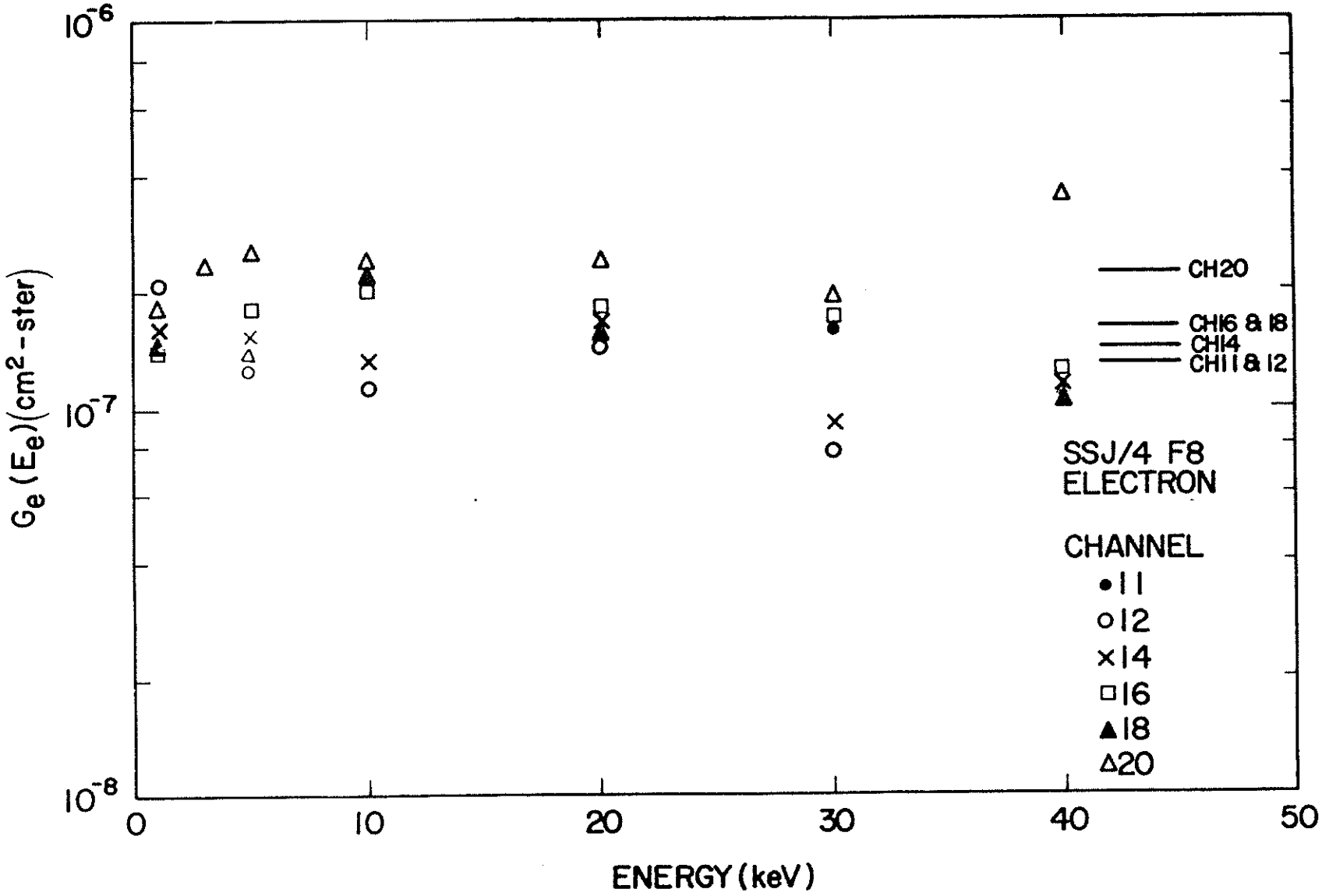

Figure 10b. The Channel Response, $G_e(E_e)$, of the Low Energy Electron Sensor to Electron Beam Energies Between 1 and 40 keV. Data were taken for Channels 11, 12, 14, 16, 18, and 20 of the SSJ/4 detector

Table 7. Electron Rejection Curve Values for the SSJ/4 F8 Electron Detector

	$G_e(E_e)$ cm^2 ster (High Energy Sensor)										
	E_e(eV)	Ch 1	Ch 2	Ch 3	Ch 4	Ch 5	Ch 6	Ch 7	Ch 8	Ch 9	Ch 10
(1)	31,300	0	1.5(-6)	5.0(-7)	2.1(-7)	1.6(-7)	1.2(-7)	9.5(-8)	7.0(-8)	5.4(-8)	3.8(-8)
(2)	21,100	3.4(-7)	0	1.1(-6)	3.4(-7)	2.0(-7)	1.3(-7)	1.0(-7)	7.4(-8)	5.7(-8)	4.0(-8)
(3)	14,300	2.1(-8)	1.6(-7)	0	7.8(-7)	2.7(-7)	1.6(-7)	1.2(-7)	8.2(-8)	6.2(-8)	4.2(-8)
(4)	9720	3.4(-9)	1.9(-8)	2.1(-7)	0	5.4(-7)	2.1(-7)	1.4(-7)	9.6(-8)	6.9(-8)	4.6(-8)
(5)	6610	1.0(-9)	3.3(-9)	2.0(-8)	2.9(-7)	0	3.6(-7)	1.9(-7)	1.2(-7)	8.0(-8)	5.4(-8)
(6)	4500	0	1.0(-9)	3.0(-9)	2.0(-8)	3.2(-7)	0	3.8(-7)	1.7(-7)	1.1(-7)	6.9(-8)
(7)	3050	0	0	0	2.7(-9)	2.0(-8)	3.5(-7)	0	3.9(-7)	1.7(-7)	9.6(-8)
(8)	2070	0	0	0	0	2.6(-9)	1.9(-8)	1.8(-7)	0	3.9(-7)	1.6(-7)
(9)	1400	0	0	0	0	0	2.6(-9)	1.9(-8)	1.2(-7)	0	3.9(-7)
(10)	950	0	0	0	0	0	0	2.5(-9)	1.8(-8)	7.5(-8)	0
	$G_e(E_e)$ cm^2 ster (Low Energy Sensor)										
	E_e(eV)	Ch 11	Ch 12	Ch 13	Ch 14	Ch 15	Ch 16	Ch 17	Ch 18	Ch 19	Ch 20
(1-10)	950 to 31,300	1.3(-7)	1.3(-7)	1.4(-7)	1.4(-7)	1.5(-7)	1.6(-7)	1.6(-7)	1.6(-7)	1.9(-7)	2.2(-7)

Note: 1.5(-6) = 1.5×10^{-6}, and so on.

6. CALIBRATION OF THE SSJ/4 PROTOTYPE ELECTRON DETECTOR

A prototype of the SSJ/4 electron detector was calibrated using the electron beam experiment at AFGL in order to check the consistency of the calibration results obtained earlier. The prototype detector is identical in design to the DMSP series F6 - F10 sensors described in Hardy et al.[18] Unlike the new F8 detector described in this report, these detectors employ two small CEMs with overlapping collecting cones instead of one CEM with a large cone.

The results of the calibration are listed in Table 8. A total of 99 angular scans was made to map response curves for channels 2, 4, 6, 10, 11, 15, 17, 19, and 20. Due to the uncertainty of the beam current measurement at very low energy, the peak geometric factor of channel 20 was set equal to the value found for channels 11, 15, 17, and 19, that is, 3.2×10^{-4} cm^2 ster. The remaining channels were assigned calibration values in a similar manner as the F8 electron detector channels discussed in Section 3.

The values of E_{peak} and ΔE of the prototype detector channels show excellent agreement with those from the F8 and F10 detectors (see Table 2 of Hardy et al[18]). The average $\Delta E/E$ is ~9 percent for the prototype detector, compared to ~ 10 percent for the F8 and F10 detectors. For the low energy sensor the peak geometric factor for the F8 and F10 detectors was approximately 2.2×10^{-4} cm^2 ster as compared to approximately 3.2×10^{-4} cm^2 ster for the prototype. For the high energy sensor the F8 and F10 peak geometric factors are within a few percent of the prototype value for channel 10. For increasing energy the difference increases with the prototype having values as much as 36 percent higher than those for the F8 and F10 detectors at 20 keV.

The width of the angular response of the prototype detector at approximately 1 keV is compared to that of the F10 detector in Table 9a. The values of channel 11 are identical, and those of channel 10 differ negligibly. The angular response of the channels in the high energy sensor is approximately constant above 1 keV, but increases with decreasing energy for the low energy sensor. Values of the full width half maximum unfocussed angle, $\Delta\beta$, are listed in Table 9b for channels 15, 17, 19, and 20 of the prototype detector. Since the peak energy-dependent geometric factor is calculated assuming beam uniformity, the decrease of $G(E)_{peak}$ at very low energies may in part be due to small but significant spreading of the beam in energy and angle. The increase in angular width we attribute primarily to the energy spread in the calibration beam perpendicular to the direction of acceleration. This width, ΔE, can be determined in the following manner.

Table 8. Channel Response Characteristics of the SSJ/4 Prototype Electron Detector

Channel	E_{peak} (eV)	ΔE (eV)	$G(E)_{peak}$ (cm^2 ster)	G (cm^2 ster eV)
1*	31,700	2820	2.7×10^{-4}	7.9×10^{-1}
2	21,500	2000	3.3×10^{-4}	6.8×10^{-1}
3*	14,600	1300	4.0×10^{-4}	5.6×10^{-1}
4	9900	860	4.7×10^{-4}	4.3×10^{-1}
5*	6730	600	5.2×10^{-4}	3.3×10^{-1}
6	4580	390	5.8×10^{-4}	2.4×10^{-1}
7*	3130	280	6.4×10^{-4}	1.8×10^{-1}
8	2140	182	7.1×10^{-4}	1.4×10^{-1}
9*	1460	130	7.6×10^{-4}	1.0×10^{-1}
10	1000	87	8.2×10^{-4}	7.3×10^{-2}
11	975	98	2.8×10^{-4}	2.7×10^{-2}
12*	665	59	3.2×10^{-4}	1.9×10^{-2}
13*	454	40	3.2×10^{-4}	1.4×10^{-2}
14*	310	28	3.2×10^{-4}	9.8×10^{-3}
15	212	22	3.3×10^{-4}	7.2×10^{-3}
16*	144	13	3.2×10^{-4}	5.0×10^{-3}
17	98	9.6	3.5×10^{-4}	3.4×10^{-3}
18*	67	6.0	3.2×10^{-4}	2.2×10^{-3}
19	46	3.7	3.3×10^{-4}	1.3×10^{-3}
20	32	2.4	3.2×10^{-4}	7.7×10^{-4}

*Channel response curve not determined by electron beam

Table 9a. The Full Width Half Maximum Angular Response, $\Delta\alpha$ and $\Delta\beta$, for the SSJ/4 Prototype and F10 Electron Detectors, Channels 10 and 11

	Channel 10			Channel 11	
	$\Delta\alpha$	$\Delta\beta$		$\Delta\alpha$	$\Delta\beta$
F 10	2.05°	8.4°	F 10	3.6°	4.5°
Electron Prototype	2.1°	8.7°	Electron Prototype	3.6°	4.5°

Table 9b. The Full Width Half Maximum Angular Response, $\Delta\beta$, for Channels 15, 17, 19, and 20 of the Low Energy SSJ/4 Prototype Electron Sensor

Electron Prototype Channel	Beam Energy (eV)	$\Delta\beta$
15	215	4.4°
17	98	5.3°
19	46	9.4°
20	32	9.5°

An electron in the calibrating beam will have an energy equal to the energy with which it was ejected from the gold surface plus the energy it obtains from acceleration by the electric field. An electron having an initial kinetic energy E_i, emitted tangent to the quartz substrate surface, will make an angle $\Delta\theta \approx \arctan (E_i/E_b)^{1/2}$ with the cathode normal after being given an energy E_b by the electric field. For such a case, the measured angular response, $\Delta\beta$, is related to the actual instrument angular response, W_{ap}, and the angular width of the calibrating beam, $\Delta\theta$, by the equation (see Marshall et al[19]),

$$\Delta\beta^2 = W_{ap}^2 + \Delta\theta^2 \quad . \tag{5}$$

For the case of $E_i/E_b \ll 1$, this equation can be approximated by

$$\Delta\beta^2 = W_{ap}^2 + E_i/E_b \quad , \tag{6}$$

so that if $\Delta\beta^2$ is plotted vs E_b^{-1}, the slope of the line gives E_i, since W_{ap}^2 is a constant. The curve derived from the values of $\Delta\beta$ vs E_b given in Table 9b is shown in Figure 11. From this the energy width of the beam $\Delta E \approx E_i$ is found to be 0.9 eV.

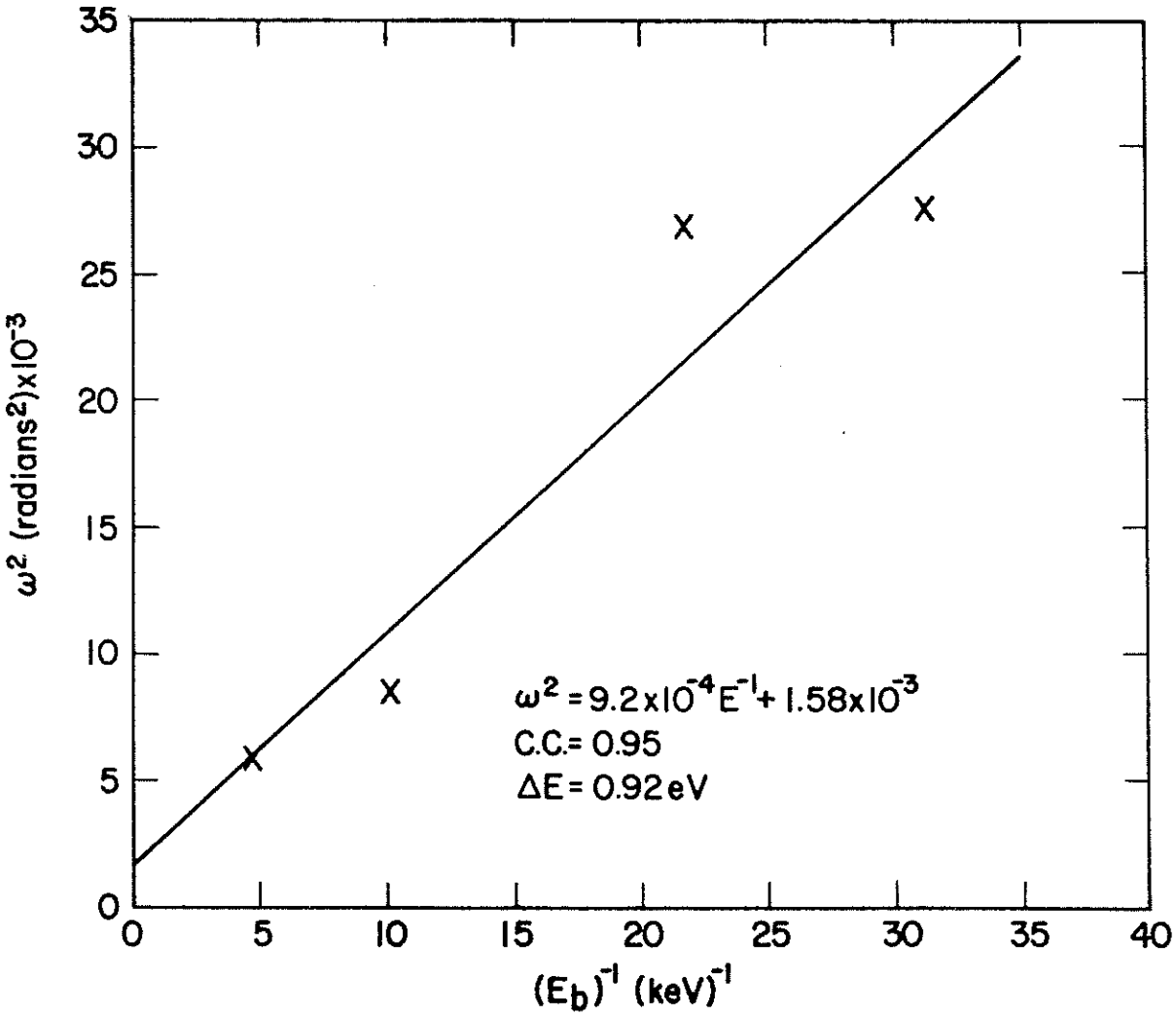

Figure 11. The Square of the Full Width Half Maximum of the Angular Response of the SSJ/4 Prototype Electron Detector Apertured CEM Plotted as a Function of the Inverse of the Electron Beam Energy. The data are from beam energies of 32, 46, 98, and 215 eV

7. CALIBRATION OF THE SSJ/4 PROTOTYPE ION DETECTOR

An additional calibration was performed to check the accuracy of the ion geometric factors assigned to the low energy sensor of the F6 and F7 detectors. The F6 and F7 values were assigned using a combination of electron calibration results and in-flight data. For this calibration, the low energy sensor of the prototype electron detector was modified to simulate the configuration of the low energy electron ion sensor with ones as used in the F6 and F7 low energy ion sensor. The plate polarity was left the same so that the electron beam facility at AFGL could be used to directly determine the low energy ion geometric factors.

Using this configuration, the characteristics of the ten ion channels of the prototype detector's low energy sensor were determined and are listed in Table 10. A total of 63 angular scans was made to map response curves for channels 11, 13, 15, 17, 19, and 20. Again, due to the uncertainty of measuring the beam current at low energies, the peak energy-dependent geometric factors of channel 19 and 20 (6.4×10^{-3} and 4.9×10^{-3} cm^2 ster, respectively) were assigned to the average $G(E)_{peak}$ of the higher energy channels (8.35×10^{-3} cm^2 ster).

Table 10. Channel Response Characteristics of the Low Energy SSJ/4 Prototype Ion Sensor

Channel	E_{peak} (eV)	ΔE (eV)	$G(E)_{peak}$ (cm^2 ster)	G (cm^2 ster eV)
11	1000	160	7.80×10^{-3}	1.25×10^{-0}
12*	682	109	8.35×10^{-3}	9.30×10^{-1}
13	465	75	9.10×10^{-3}	6.90×10^{-1}
14*	318	51	8.35×10^{-3}	4.35×10^{-1}
15	218	35	8.50×10^{-3}	3.10×10^{-1}
16*	149	24	8.35×10^{-3}	2.05×10^{-1}
17	102	17	8.00×10^{-3}	1.40×10^{-1}
18*	69	11	8.35×10^{-3}	9.40×10^{-2}
19	47	7.5	8.35×10^{-3}	6.30×10^{-2}
20	33	5.0	8.35×10^{-3}	4.45×10^{-2}

*Channel response curve not determined by electron beam

The values of E_{peak} of the low energy prototype ion sensor channels show excellent agreement with those values of the F6 and F7 low energy ion sensor channels (see Table 3 of Hardy et al[18]), but the channel widths differ significantly. All channels of the F6 and F7 detectors were assigned to the same value of $\Delta E/E$ as determined from the electron channels ($\approx$ 10 percent). However, the experimentally determined values of $\Delta E/E$ for the prototype ion channels averaged 16 percent. The wider channel bands result from the ion aperture being larger than the electron aperture.

Due in part to the underestimation of ΔE, the values of $G(E)_{peak}$ for the F6 and F7 ion detector channels are larger by about a factor of three than those found for the prototype ion detector. $G(E)_{peak}$ had been assigned using F6 and F7 ion flight data assuming that channels 10 and 11 should record counts proportional to the ratio of the products of their respective values of $G(E)_{peak}$ and ΔE. If the peak energy-dependent geometric factors for the F6 and F7 ion detectors were to be recalculated using $\Delta E/E$ = 16 percent rather than 10 percent, the new values would differ from the values of $G(E)_{peak}$ for the low energy prototype ion sensor by about a factor of two. The reason for the large discrepancy is not known and will be investigated in future calibrations.

The increase in aperture size of the low energy ion sensor was found to increase the channels' angular response width, as well as their energy band width, in relation to the low energy electron sensor. $\Delta\alpha$ and $\Delta\beta$ of channel 11 of the prototype ion detector are 8.4° and 8.0°, respectively, compared to the prototype electron detector's values of 3.6° and 4.5°, respectively. As expected, the angular response width was also found to increase with decreasing beam energy. Values of $\Delta\beta$ are listed in Table 11 for six channels of the low energy prototype ion sensor. A linear fit of $\Delta\beta^2$ vs the inverse of the beam energy indicates a beam width of 0.9 eV, consistent with the results using data from the SSJ/4 prototype electron detector.

Table 11. The Full Width Half Maximum Unfocussed Angular Response, $\Delta\beta$, for Channels 11, 13, 15, 17, 19, and 20 of the Low Energy SSJ/4 Prototype Ion Sensor

Ion Prototype Channel	Beam Energy (eV)	$\Delta\beta$
11	1000	8.0°
13	415	10.1°
15	221	11.2°
17	100	11.2°
19	47	13.3°
20	33	12.7°

8. SURVEY PLOTS

For each DMSP F8 satellite pass the following quantities are calculated and plotted as a function of universal time for electron and ion data surveys:

(a) The summation,

$$S(E_1)(E_1 - E_2) + \sum_{i=2}^{9} S(E_i)(E_{i-1} - E_{i+1})/2$$

$$+ 1/2[S(E_{10}) + S(E_{11})][(E_9 - E_{12})/2] + \sum_{i=12}^{19} S(E_i)(E_{i-1} - E_{i+1})/2$$

$$+ S(E_{20})(E_{19} - E_{20}) \quad . \tag{7}$$

gives (1) the total integral number flux, JTOT, when $S(E_i) = J(E_i)$, where $J(E_i)$ is the differential number flux for each energy channel with central energy E_i, or (2) the total integral energy flux, JETOT, when $S(E_i) = E_i J(E_i)$. JTOT is measured in particles/(cm^2 ster sec) and JETOT is measured in keV/(cm^2 ster sec).

By substituting Eq. (3) into Eq. (7), each term of the summation may be written as the number of counts, C_i, within each energy channel, i, multiplied by a coefficient, $K(E_i)$, such that

$$JTOT = \sum_{i=1}^{9} K_{JTOT}(E_i) C_i + 1/2[K_{JTOT}(E_{10}) C_{10} + K_{JTOT}(E_{11}) C_{11}]$$

$$+ \sum_{i=12}^{20} K_{JTOT}(E_i) C_i \quad , \tag{8}$$

where $K_{JTOT}(E_1) = (E_1 - E_2)/(\Delta T G_1)$, $K_{JTOT}(E_{10}) = (E_9 - E_{12})/(2\Delta T G_{10})$, $K_{JTOT}(E_{11}) = (E_9 - E_{12})/(2\Delta T G_{11})$, $K_{JTOT}(E_{20}) = (E_{19} - E_{20})/(\Delta T G_{20})$, and for all other i, $K_{JTOT}(E_i) = (E_{i+1} - E_{i-1})/(2\Delta T G_i)$. Also,

$i-1 \qquad i+1$

$$JETOT = \sum_{i=1}^{9} K_{JETOT}(E_i) C_i + 1/2 \sum_{i=10}^{11} K_{JETOT}(E_i) C_i$$

$$+ \sum_{i=12}^{20} K_{JETOT}(E_i) C_i \ , \qquad (9)$$

where $K_{JETOT}(E_i) = E_i K_{JTOT}(E_i)$. The values for $K_{JTOT}(E_i)$ and $K_{JETOT}(E_i)$ are given for both ions and electrons in Table 12.

(b) The average energy, EAVE, is

$$EAVE = JETOT/JTOT \ . \qquad (10)$$

EAVE is measured in keV.

Figure 12 is an example of survey plots for electrons (12a) and ions (12b) during a north polar pass of the F8 satellite on 26 June 1987, from 17:59 to 18:22 UT. The universal time is given in seconds and hr:min:sec with an interval of 1-min between tick marks. At 2-min intervals ephemeris data are given. The ephemerides include the geographic coordinates of the satellite (GLAT and GLON); the corrected geomagnetic coordinates of the satellite (MLAT and MLON), which are projected along the magnetic field line to 110 km; and the magnetic local time (MLT). The integral and energy flux values are plotted on log scales; the average energy is plotted on a linear scale. The satellite crosses the high latitude region from approximately 5 MLT, or predawn, to 19 MLT, or post-dusk, during disturbed geomagnetic conditions. The survey plots show the morning diffuse auroral precipitation rising out of the background, with the equatorward electron boundary of the diffuse aurora being lower in latitude than the ion boundary. A discrete auroral structure is located on the poleward morningside edge of the diffuse aurora. Very low fluxes mark clear entry into the polar cap. After approximately 4 min in the cap the satellite again crosses the eveningside auroral oval. The evening oval is wider and the electron precipitation more intense and structured than that on the morningside.

Table 12. Coefficients Used to Calculate the Total Integral Number Flux, JTOT, and the Total Integral Energy Flux, JETOT, for Ions and Electrons

Channel	SSJ/4 F8			
	JTOT Coefficient $(cm^2\ ster\ sec)^{-1}$		JETOT Coefficient $keV/(cm^2\ ster\ sec)$	
	Electrons	Ions	Electrons	Ions
1	1.95×10^5	3.78×10^4	6.09×10^6	1.18×10^6
2	1.89×10^5	4.82×10^4	3.99×10^6	1.02×10^6
3	1.62×10^5	4.84×10^4	2.32×10^6	6.92×10^5
4	1.48×10^5	5.03×10^4	1.44×10^6	4.89×10^5
5	1.16×10^5	4.80×10^4	7.65×10^5	3.17×10^5
6	9.82×10^4	4.66×10^4	4.42×10^5	2.10×10^5
7	8.27×10^4	4.86×10^4	2.52×10^5	1.48×10^5
8	6.73×10^4	5.10×10^4	1.39×10^5	1.06×10^5
9	6.14×10^4	4.96×10^4	8.60×10^4	6.96×10^4
10	4.91×10^4	4.91×10^4	4.66×10^4	4.66×10^4
11	6.92×10^4	1.69×10^3	6.57×10^4	1.61×10^3
12	6.27×10^4	1.68×10^3	4.01×10^4	1.08×10^3
13	6.48×10^4	1.60×10^3	2.85×10^4	7.04×10^2
14	6.34×10^4	1.56×10^3	1.97×10^4	4.84×10^2
15	6.27×10^4	1.66×10^3	1.32×10^4	3.49×10^2
16	6.88×10^4	1.66×10^3	9.91×10^3	2.39×10^2
17	6.69×10^4	1.62×10^3	6.56×10^3	1.59×10^2
18	6.76×10^4	1.64×10^3	4.60×10^3	1.12×10^2
19	6.99×10^4	1.72×10^3	3.15×10^3	7.74×10^1
20	7.72×10^4	1.90×10^3	2.39×10^3	5.90×10^1

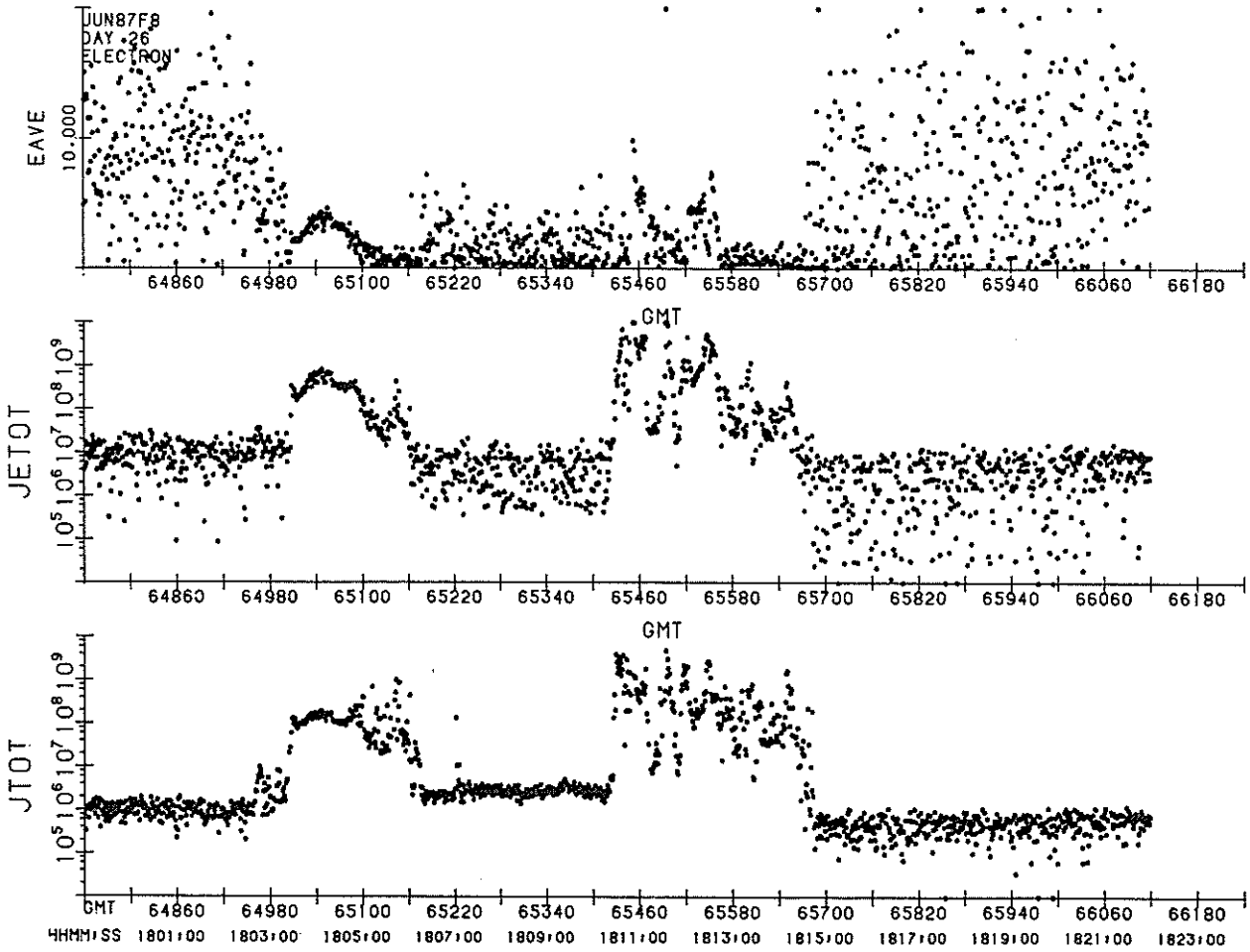

GLAT	61.5	68.0	74.2	79.2	81.1	78.2	72.7	66.5	59.8	53.1	46.2	0.0
GLON	166.0	159.4	148.3	126.0	85.0	48.2	29.5	19.9	14.0	9.9	6.8	0.0
MLAT	57.4	63.3	68.8	73.0	74.8	73.6	69.8	64.6	58.6	52.1	45.3	0.0
MLON	228.0	220.1	207.9	189.0	163.2	136.8	116.9	103.9	95.2	88.9	84.2	0.0
MLT	4.7	4.2	3.4	2.2	0.5	22.8	21.5	20.6	20.1	19.7	19.4	0.0

Figure 12a. Electron Data From a Northern Hemisphere Pass of the F8 Satellite Occurring Between 17:59 UT (64,740 sec) and 18:22 UT (66,120 sec) on 26 June 1987. The three panels give, from top to bottom, the average electron energy, EAVE, in units of keV plotted on a linear scale, the integrated energy flux, JETOT, in units of keV/(cm^2 ster sec) plotted on a logarithmic scale; and the integrated number flux, JTOT, in units of electrons/(cm^2 ster sec) plotted on a logarithmic scale. The bottom of each figure is annotated with the universal time in seconds and hr:min:sec, the geographic and geomagnetic coordinates of the satellite mapped down the field line to 110 km, and the geomagnetic local time

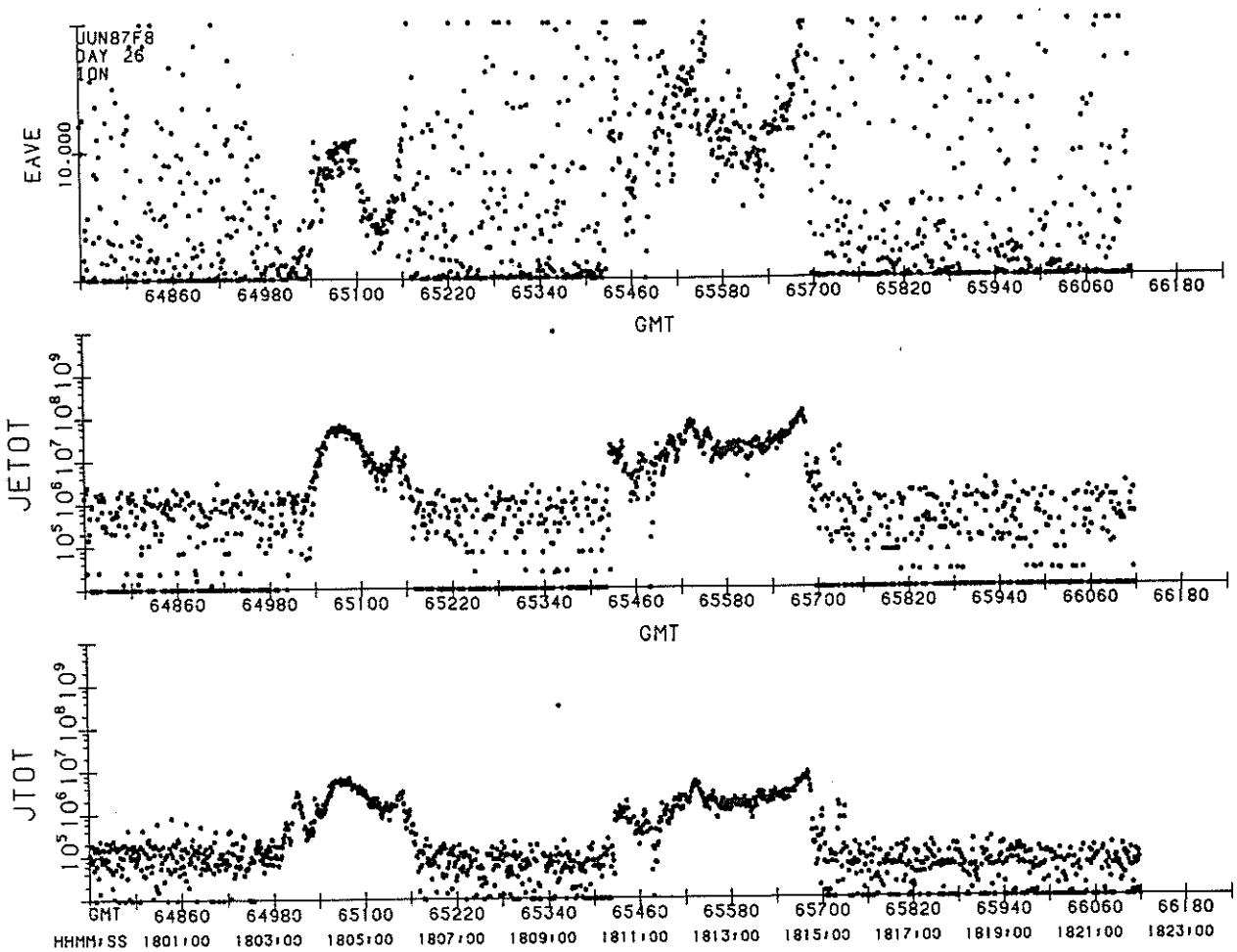

GLAT	61.5	68.0	74.2	79.2	81.1	78.2	72.7	66.5	59.8	53.1	46.2	0.0
GLON	166.0	159.4	148.3	126.0	85.0	48.2	29.5	19.9	14.0	9.9	6.8	0.0
MLAT	57.4	63.3	68.8	73.0	74.8	73.6	69.8	64.6	58.6	52.1	45.3	0.0
MLON	228.0	220.1	207.9	189.0	163.2	136.8	116.9	103.9	95.2	88.9	84.2	0.0
MLT	4.7	4.2	3.4	2.2	0.5	22.8	21.5	20.6	20.1	19.7	19.4	0.0

Figure 12b. Ion Data From a Northern Hemisphere Pass of the F8 Satellite Occurring Between 17:59 UT (64,740 sec) and 18:22 UT (66,120 sec) on 26 June 1987. The three panels give, from top to bottom, the average ion energy, EAVE, in units of keV plotted on a linear scale; the integrated energy flux, JETOT, in units of keV/(cm^2 ster sec) plotted on a logarithmic scale; and the integrated number flux, JTOT, in units of ions/(cm^2 ster sec) plotted on a logarithmic scale. The bottom of each figure is annotated with the universal time in seconds and hr:min:sec, the geographic and geomagnetic coordinates of the satellite mapped down the field line to 110 km, and the geomagnetic local time

9. USE OF ELECTRON REJECTION CURVES FOR THE ELECTRON AND ION CHANNELS

In the following we present two examples of the use of the electron rejection curves to correct electron and ion spectra. The examples are from the 26 June 1987 pass shown in Figure 12 and described in the previous section. Figure 12a shows discrete arcs near the poleward edge of the eveningside auroral oval. The arcs have inverted-V structure with individual spectra showing evidence of field-aligned acceleration characterized by an enhancement of $\geqq$ 1 keV electrons. In Figures 13 and 14 the measured and corrected electron and ion spectra within the enhancement region are shown. The two sets of spectra are observed approximately 10 sec UT apart. One notes that there is a large increase in the 1 keV electron flux shown in Figure 13a, likewise in the 10 keV electron flux in Figure 14a. The measured, rejected, and corrected counts for the 20 electron and ion channels are listed in Tables 13 and 14. For the electron spectrum peaked at 1 keV, Table 13 shows that the rejected counts due to electron scattering (1) are comparable to or greater than the measured counts for the $\leqq$ 300 eV electron energy channels, and (2) comprise an average of 60 percent of the measured counts for the $\leqq$ 300 eV ion energy channels. For the electron spectra peaked at 10 keV, Table 14 shows that the rejected counts (1) are greater than the measured counts for the $\leqq$ 100 eV electron energy channels, (2) comprise an average of 40 percent of the measured counts for the electron energy channels between 0.1 and 1 keV, and (3) account for nearly all the measured counts in the ion energy channels. In auroral regions where field-aligned acceleration is absent, Hardy et al[18] have shown that the correction to measured particle counts is 10 percent or less.

That the rejected electron counts in Table 13 are significantly greater than the measured counts in the low energy electron sensor is cause for concern. During the calibration experiment, the response curves of channels with central energies between 200 and 500 eV were inconsistent and difficult to reproduce; no channel response was measured below 200 eV. We attributed these results to problems maintaining a steady electron beam. However, since the in-flight data suggest that electron counts measured by the low energy sensor are too small, we can not rule out the possibility that the results are due to instrument-related problems. This matter will be investigated in future calibration experiments.

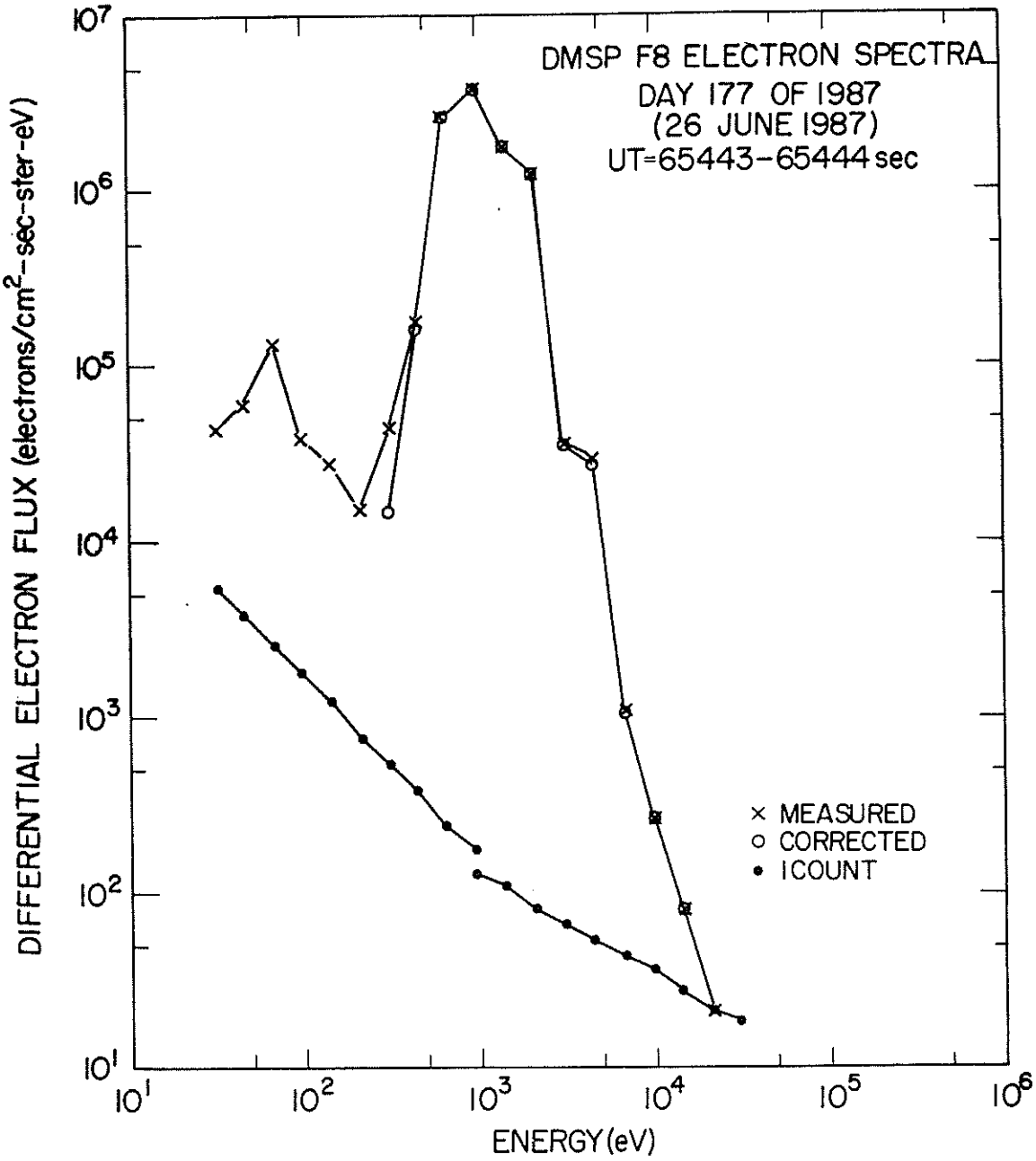

Figure 13a. The SSJ/4 F8 Differential Number Flux Spectra for Electrons at 65,443 - 65,444 sec UT on 26 June 1987. Shown are the measured electron spectrum (x), corrected electron spectrum for electron scattering through the analyzer (o), and the one count level for electrons (·)

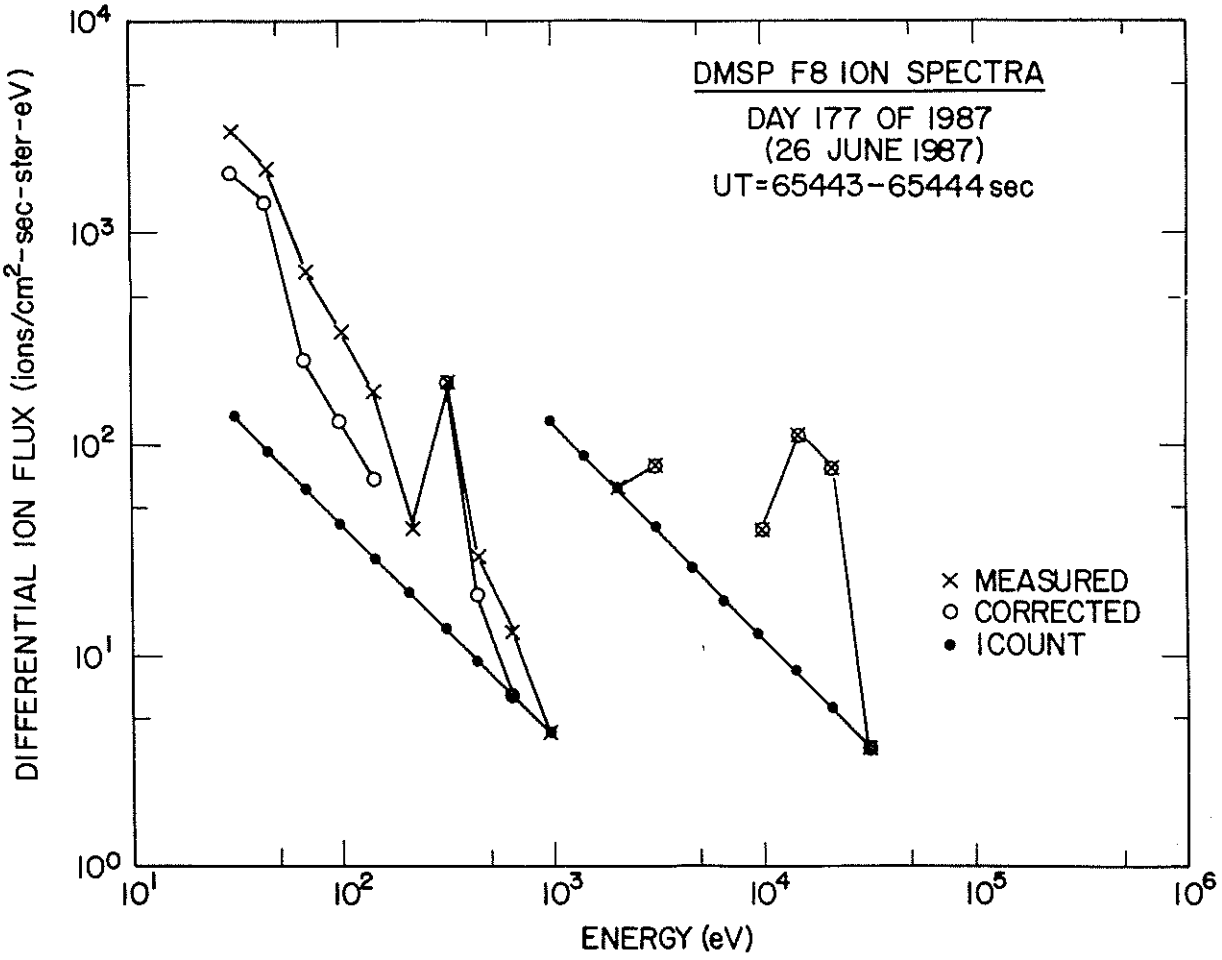

Figure 13b. The SSJ/4 F8 Differential Number Flux Spectra for Ions at 65,443 - 65,444 sec UT on 26 June 1987. Shown are the measured ion spectrum (x), corrected ion spectrum for electron scattering through the analyzer (o), and the one count level for ions (·)

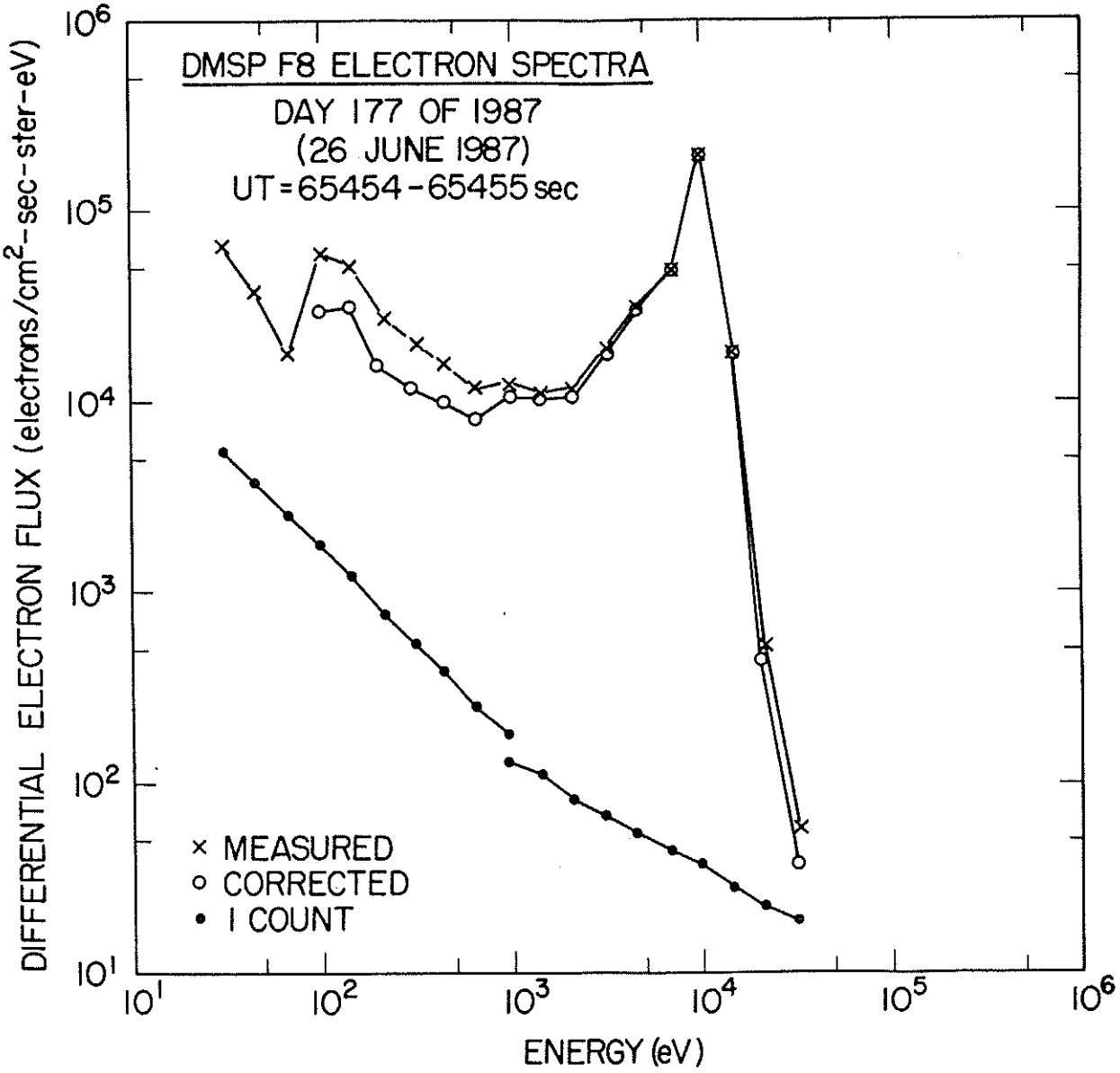

Figure 14a. The SSJ/4 F8 Differential Number Flux Spectra for Electrons at 65,454 - 65,455 sec UT on 26 June 1987. Shown are the measured electron spectrum (x), corrected electron spectrum for electron scattering through the analyzer (o), and the one count level for electrons (·)

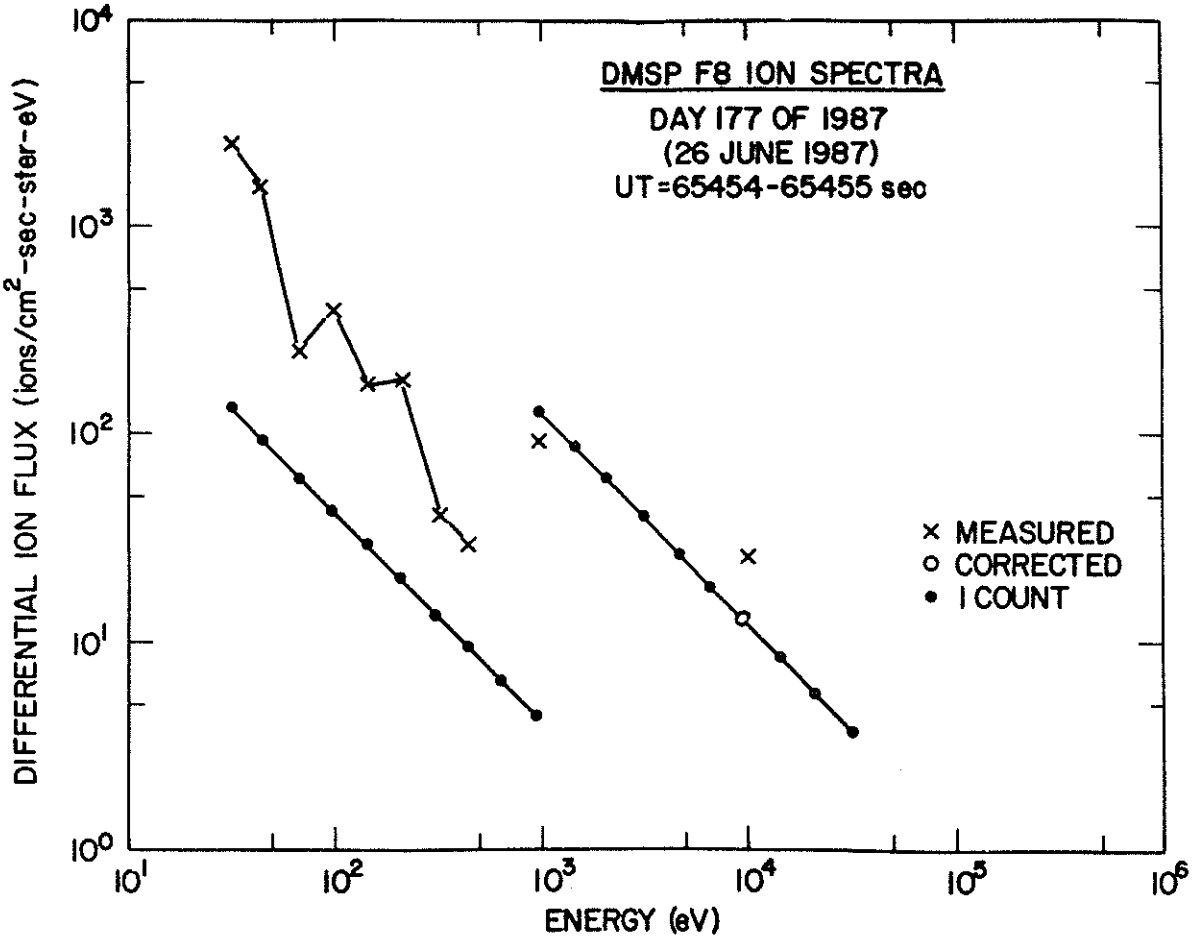

Figure 14b. The SSJ/4 F8 Differential Number Flux Spectra for Ions at 65,454 - 65,455 sec UT on 26 June 1987. Shown are the measured ion spectrum (x), corrected ion spectrum for electron scattering through the analyzer (o), and the one count level for ions (•)

Table 13. Measured, Rejected, and Corrected Electron and Ion Counts for Spectra at 65,443 - 65,444 sec UT on 26 June 1987

UT = 65,443 to 65,444 sec (18:10:43 to 18:10:44)						
	Electrons			Ions		
Channel No.	Cts_m	Cts_r	Cts_c	Cts_m	Cts_r	Cts_c
1	0	0	0	1	0	1
2	1	0	1	14	0	14
3	3	0	3	13	0	13
4	7	0	7	3	0	3
5	26	1	25	0	0	0
6	55	4	51	0	0	0
7	543	21	522	2	0	0
8	15,583	16	15,567	1	1	0
9	16,351	51	16,300	0	1	0
10	29,151	55	29,096	0	1	0
11	20,959	45	20,914	1	1	0
12	10,719	45	10,674	2	1	1
13	455	49	406	3	1	2
14	81	49	32	15	1	14
15	21	52	0	2	2	0
16	22	55	0	6	4	2
17	22	55	0	8	5	3
18	53	55	0	11	7	4
19	16	66	0	22	7	15
20	8	76	0	22	8	14

Cts_m = measured counts;

Cts_r = rejected counts;

Cts_c = corrected counts.

Table 14. Measured, Rejected, and Corrected Electron and Ion Counts for Spectra at 65,454 - 65,455 sec UT on 26 June 1987

UT = 65,454 to 65,455 sec (18:10:54 to 18:10:55)						
	Electrons			Ions		
Channel No.	Cts_m	Cts_r	Cts_c	Cts_m	Cts_r	Cts_c
1	3	1	2	0	0	0
2	23	3	20	0	0	0
3	655	16	639	0	0	0
4	5087	12	5075	2	1	1
5	1119	45	1074	0	1	0
6	575	23	552	0	1	0
7	279	16	263	0	1	0
8	143	11	132	0	1	0
9	103	8	95	0	1	0
10	93	6	87	2	2	0
11	69	14	55	5	13	0
12	47	14	33	0	14	0
13	41	15	26	3	15	0
14	37	15	22	3	17	0
15	37	16	21	9	18	0
16	43	17	26	6	20	0
17	35	17	18	9	20	0
18	7	17	0	4	21	0
19	10	20	0	17	21	0
20	12	24	0	19	21	0

Cts_m = measured counts;

Cts_r = rejected counts;

Cts_c = corrected counts.

References

1. Hardy, D.A., Gussenhoven, M.S., and Huber, A. (1979) The Precipitating Electron Detectors (SSJ/3) for the Block 5D/Flights 2 - 5 DMSP Satellites: Calibration and Data Reduction, AFGL-TR-79-0210, ADA 083136, Air Force Geophysics Laboratory, Hanscom AFB, MA.
2. Hardy, D.A., Gussenhoven, M.S., and Holeman, E. (1985) A statistical model of auroral electron precipitation, J. Geophys. Res., 90:4229.
3. Hardy, D.A., Gussenhoven, M.S., and Brautigam, D. (1988) A statistical model of auroral ion precipitation, to be published in J. Geophys. Res.
4. Gussenhoven, M.S., Hardy, D.A., and Burke, W.J. (1981) DMSP/F2 electron observations of equatorward auroral boundaries and their relationship to magnetospheric electric fields, J. Geophys. Res., 86:768.
5. Gussenhoven, M.S., Hardy, D.A., and Heinemann, N. (1983) Systematics of the equatorward diffuse auroral boundary, J. Geophys. Res., 88:5692.
6. Gussenhoven, M.S., Hardy, D.A., and Heinemann, N. (1987) The equatorward boundary of auroral ion precipitation, J. Geophys. Res., 92:8273.
7. Hardy, D.A., Burke, W.J., Gussenhoven, M.S., Heinemann, N., and Holeman, E. (1981) DMSP/F2 electron observations of equatorward auroral boundaries and their relationship to the solar wind velocity and the north-south component of the interplanetary magnetic field, J. Geophys. Res., 86:9961.
8. Hardy, D.A., and MacKean, R. (1980) An Algorithm for Determining the Boundary of Auroral Precipitation Using Data from the SSJ/3 Sensor, AFGL-TR-80-0028, ADA 084482, Air Force Geophysics Laboratory, Hanscom AFB, MA.

9. Gussenhoven, M.S., Hardy, D.A., Heinemann, N., and Holeman, E. (1982) 1978 Diffuse Auroral Boundaries and a Derived Auroral Boundary Index, AFGL-TR-82-0398, ADA 130175, Air Force Geophysics Laboratory, Hanscom AFB, MA.

10. Gussenhoven, M.S., Hardy, D.A., Heinemann, N., and Burkhardt, R. (1984) Morphology of the polar rain, J. Geophys. Res., 89:9785.

11. Gussenhoven, M.S., Hardy, D.A., and Carovillano, R.L. (1985a) Average electron precipitation in the polar cusps, cleft, and cap in The Polar Cusp, (J.A. Holtet and A. Egeland, Eds.), D. Reidel Pub. Co., Holland, p. 85.

12. Hardy, D.A. (1984) Intense fluxes of low-energy electrons at geomagnetic latitudes above 85°, J. Geophys. Res., 89:3883.

13. Hardy, D.A., Gussenhoven, M.S., Riehl, K., Burkhardt, R., Heinemann, N., and Schumaker, T.L. (1986) The characteristics of polar cap precipitation and their dependence on the interplanetary magnetic field and the solar wind, in Solar Wind-Magnetospheric Coupling, (Y. Kamide and J.A. Slavin, Eds.), Terra Sci. Pub. Co., Tokyo, p. 575.

14. Riehl, K.B., and Hardy, D.A. (1986) Average characteristics of the polar rain and their relationship to the solar wind and interplanetary magnetic field, J. Geophys. Res., 91:1557.

15. Schumaker, T.L., Gussenhoven, M.S., and Hardy, D.A. (1984) Ion signatures in the polar rain, EOS Trans. Am. Geophys. Union, 65:1065.

16. Gussenhoven, M.S., Hardy, D.A., Rich, F., Burke, W.J., and Yeh, H.-C. (1985b) High-level spacecraft charging in the low-altitude polar auroral environment, J. Geophys. Res., 90:11,009.

17. Yeh, H.-C, and Gussenhoven, M.S. (1987) The statistical electron environment for DMSP charging, J. Geophys. Res., 92:7705.

18. Hardy, D.A., Schmitt, L.K., Gussenhoven, M.S., Marshall, F.J., Yeh, Y.-C., Schumaker, T.L., Huber, A., and Pantazis, J. (1984) Precipitating Electron and Ion Detectors (SSJ/4) for the Block 5D/Flights 6 - 10 DMSP Satellites: Calibration and Data Presentation, AFGL-TR-84-0317, ADA 157080, Air Force Geophysics Laboratory, Hanscom AFB, MA.

19. Marshall, F.J., Hardy, D.A., Huber, A., Pantazis, J., McGarity, J., Holeman, E., and Winningham, J.D. (1986) Calibration system for electron detectors in the energy range from 10 eV to 50 keV, Rev. Sci. Instrum., 57(No. 2):229.

☆U.S. GOVERNMENT PRINTING OFFICE: 1989-600-431/80110